



OLD DOMINION UNIVERSITY RESEARCH FOUNDATION

(NASA-CR-16999) IMPORTANCE OF RADIATIVE
HEATING FOR A TITAN AEROCAPTURE MISSION
Final Report, 30 Jun. - 30 Oct. 1980 (Old
Dominion Univ., Norfolk, Va.) 54 p

N83-74554

Unclass
00/12 15315

DEPARTMENT OF MECHANICAL ENGINEERING AND MECHANICS
SCHOOL OF ENGINEERING
OLD DOMINION UNIVERSITY
NORFOLK, VIRGINIA

IMPORTANCE OF RADIATIVE HEATING FOR A TITAN AEROCAPTURE MISSION

By

S.N. Tiwari, Principal Investigator

and

H. Chow

Final Report

For the period June 30, 1980 to October 30, 1980

Prepared for the
National Aeronautics and Space Administration
Langley Research Center
Hampton, Virginia

Under
Research Grant NAS1-15648
Task Authorization No. 39
James N. Moss and James J. Jones, Technical Monitors
Space Systems Division

REPRODUCED BY
NATIONAL TECHNICAL
INFORMATION SERVICE
U.S. DEPARTMENT OF COMMERCE
SPRINGFIELD, VA. 22161

December 1982

DEPARTMENT OF MECHANICAL ENGINEERING AND MECHANICS
SCHOOL OF ENGINEERING
OLD DOMINION UNIVERSITY
NORFOLK, VIRGINIA

IMPORTANCE OF RADIATIVE HEATING FOR A
TITAN AEROCAPTURE MISSION

By

S.N. Tiwari, Principal Investigator

and

H. Chow

Final Report

For the period June 30, 1980 to October 30, 1980

Prepared for the
National Aeronautics and Space Administration
Langley Research Center
Hampton, Virginia 23665

Under
Research Grant NAS1-15648
Task Authorization No. 39
James N. Moss and James J. Jones, Technical Monitors
Space Systems Division

Submitted by the
Old Dominion University Research Foundation
P.O. Box 6369
Norfolk, Virginia 23508-0369



December 1982

TABLE OF CONTENTS

	<u>Page</u>
PREFACE.....	vi
SUMMARY.....	1
LIST OF SYMBOLS.....	1
INTRODUCTION.....	3
BASIC FORMULATION.....	4
Equilibrium Gas Composition.....	9
Radiation Transport Model.....	10
PHYSICAL CONDITIONS AND DATA SOURCE.....	10
Entry Trajectory and Freestream Conditions.....	11
Chemical Composition of Gas Mixture.....	11
Thermodynamic and Transport Properties.....	18
METHOD OF SOLUTION.....	18
RESULTS AND DISCUSSION.....	18
CONCLUSIONS.....	44
REFERENCES.....	47

LIST OF TABLES

Table

1	Altitude and freestream conditions: Trajectory I ($L/D = 1.2$, $\gamma = -45^\circ$, $\beta = 800 \text{ kg/m}^2$, $U_E = 10 \text{ km/s}$).....	13
2	Altitude and freestream conditions: Trajectory II ($L/D = 1.2$, $\gamma = -25^\circ$, $\beta = 800 \text{ kg/m}^2$, $U_E = 10 \text{ km/s}$).....	14
3	Altitude and freestream conditions: Trajectory III ($L/D = 1.2$, $\gamma = -45^\circ$, $\beta = 800 \text{ kg/m}^2$, $U_E = 6 \text{ km/s}$).....	15
4	Altitude and freestream conditions: Trajectory IV ($L/D = 1.2$, $\gamma = -45^\circ$, $\beta = 800 \text{ kg/m}^2$, $U_E = 8 \text{ km/s}$).....	16
5	Altitude and freestream conditions: Trajectory V ($L/D = 1.2$, $\gamma = -45^\circ$, $\beta = 800 \text{ kg/m}^2$, $U_E = 13 \text{ km/s}$).....	17

LIST OF TABLES - CONCLUDED

<u>Table</u>		<u>Page</u>
6	Stagnation results (sphere cone, $R_N = 0.2$ m, $T_w = 2,000$ K): atmosphere - 99.5% N_2 + 0.5% CH_4 , Trajectory I.....	20
7	Stagnation results (sphere cone, $R_N = 0.2$ m, $T_w = 2,000$ K): atmosphere - 90% N_2 + 10% CH_4	22

LIST OF FIGURES

<u>Figure</u>		
1(a)	Titan aerocapture vehicle configuration.....	5
1(b)	Coordinate system.....	6
2	The altitude history for an aerocapture vehicle.....	12
3	Variation in mole fraction of different species for $P = 1.0$ atm and 90% N_2 + 10% CH_4	19
4	Effect of gas composition on stagnation-point shock temperature, Trajectory I.....	25
5	Effect of gas composition on temperature distribution along the stagnation streamline, Trajectory I (time = 78 s).....	26
6	Effect of gas composition on stagnation-point convective heating, Trajectory I.....	27
7	Effect of gas composition on stagnation-point radiative heating.....	28
8	Variation of stagnation-point shock temperature and convective and radiative heating for 99.5% N_2 + 0.5% CH_4 ...	29
9	Effect of entry velocity on stagnation-point shock temperature, 90% N_2 + 10% CH_4	31
10	Effect of entry velocity on stagnation-point convective heating, 90% N_2 + 10% CH_4	32
11(a)	Effect of entry velocity on stagnation-point radiative heating, 90% N_2 + 10% CH_4	33
11(b)	Effect of entry velocity on stagnation-point radiative heating, 99.5% N_2 + 0.5% CH_4	34

LIST OF FIGURES - CONCLUDED

<u>Figure</u>		<u>Page</u>
12	Variation of stagnation point convective and radiative heating for Trajectories I and II, 90% N ₂ + 10% CH ₄	35
13	Effect of body nose radius on stagnation-point convective and radiative heating for 99.5% N ₂ + 0.5% CH ₄ , t = 78 s....	36
14	Variation of shock temperature, convective and radiative heating along the body for 99.5% N ₂ + 0.5% CH ₄	38
15(a)	Influence of CN on convective and radiative heating along the body for t = 78 s and 90% N ₂ + 10% CH ₄	39
15(b)	Influence of CN on convective and radiative heating along the body for t = 78 s and 99.5% N ₂ + 0.5% CH ₄	40
16	Variation of shock density and shock-standoff distance with body coordinate for 99.5% N ₂ + 0.5% CH ₄	41
17	Variation of shock temperature and enthalpy with body coordinate for 99.5% N ₂ + 0.5% CH ₄	42
18	Variation of convective and radiative heating along the body for 99.5% N ₂ + 0.5% CH ₄	43
19	Variation of convective and radiative heating along the body for Trajectory I, 90% N ₂ + 10% CH ₄ (t = 78 s), and Trajectory VI, 90% N ₂ + 2% CH ₄ (t = 78 s).....	45

PREFACE

This report covers the work completed under the NASA/Langley Contract NAS1-15648, Task Authorization No. 39. The period of performance for this task was four months (June 30, 1980 through October 30, 1980). Since the expiration of the contract, additional research was conducted under a separate project entitled "Analysis of the Aerothermodynamic Environment of a Titan Aerocapture Vehicle." Some basic findings of these studies are presented in this report. Both projects were monitored by James N. Moss and Jim J. Jones, Mail Stop 366, NASA/Langley Research Center, Hampton, Virginia.

IMPORTANCE OF RADIATIVE HEATING FOR A TITAN AEROCAPTURE MISSION

By

S.N. Tiwari¹ and H. Chow²

SUMMARY

The extent of convective and radiative heating for a Titan entry vehicle is investigated. The flow in the shock layer is assumed to be axisymmetric, steady, laminar, viscous, and in chemical and local thermodynamic equilibrium. The implicit finite difference technique is used to solve the viscous shock-layer equations for an equivalent body which is a 45° sphere cone at zero angle of attack. Different compositions for the Titan's $N_2 - CH_4$ atmosphere were assumed, and results were obtained for the entry conditions specified by the Jet Propulsion Laboratory. The results show that the heating rates, in general, increase with increasing N_2 concentration. Both convective and radiative heating increase with increasing initial entry velocity. The radiative heating increases but the convective heating decreases with increasing body nose radius. The amount of CN concentration in the shock-layer gas determines the extent of radiative heating to the body. Radiative heating will be important for freestream gas compositions with N_2 concentration between 50% and 90%. For the atmospheric composition of 99.5% $N_2 + 0.5\% CH_4$, the radiative heating is insignificant in comparison to the convective heating.

LIST OF SYMBOLS

C_i	mass fraction of species i in the shock layer, ρ_i/ρ
C_p	equilibrium specific heat of mixture, $\sum C_i C_{p,i}$
$C_{p,i}$	specific heat of specific i , $C_{p,i}^*/C_{p,\infty}^*$

¹Eminent Professor, Department of Mechanical Engineering and Mechanics, Old Dominion University, Norfolk, Virginia 23508.

²Graduate Research Assistant, Department of Mechanical Engineering and Mechanics, Old Dominion University, Norfolk, Virginia 23508.

D_{ij}	binary diffusion coefficient
h_i	specific enthalpy, h^*/V_∞^{*2}
J_i	mass diffusion flux of species i , $J_i^* R_N / \mu_{ref}^*$
k	thermal conductivity of mixture, $k^* / \mu^* C_{ref}^* C_{p,\infty}^*$
L/D	lift/drag
Le	Lewis number, $\rho^* D_{ij}^* C_p^* / k^*$
M_i^*	molecular weight of species i
\bar{M}^*	molecular weight of mixture
n	coordinate normal to the body, n^* / R_N^*
p	pressure, $p^* / (\rho_\infty^* V_\infty^{*2})$
Pr	Prandtl number, $\mu^* C_p^* / k^*$
q_r	net radiant heat flux, $q_r^* / (\rho_\infty^* V_\infty^{*3})$
r	radius measured from axis of symmetry to a point on the body surface, r^* / R_N^*
R^*	universal gas constant
R_D^*	radius of the body
Re_∞	Reynolds number, $\rho_\infty^* V_\infty^* R_N / \mu_\infty^*$
R_N^*	body nose radius
s	coordinate along the body surface, s^* / R_N^*
T	temperature, T^* / T_{ref}^*
T_{ref}^*	reference temperature, $V_\infty^{*2} / C_{p,\infty}^*$
u	velocity tangent to body surface, u^* / V_∞^*
U_E	initial entry velocity
v	velocity normal to body surface, v^* / V_∞^*
V_∞^*	freestream velocity
α	shock angle

β	ballistic coefficient, $(W/C_D A)$
γ	inertial entry angle
ϵ	Reynolds number parameter
θ	body angle
κ	body curvature, $\kappa^* R_N^*$
μ	viscosity of mixture, μ^*/μ_{ref}^*
μ_{ref}^*	reference viscosity, $\mu^*(T_{ref}^*)$
ρ	density of mixture, ρ^*/ρ_{∞}^*

Subscripts

i	ith species
s	shock value
w	wall value
∞	freestream condition

INTRODUCTION

The feasibility of aerocapture vehicle mission has been emphasized recently for inner and outer planetary mission (refs. 1-6). The aerocapture vehicle essentially is a contoured heat shield that encloses the planetary orbital spacecraft and its subsystems. The vehicle has a communication system that reaches the Earth through interface with spacecraft electronics. Originally, the aerocapture study was undertaken for a Mars sample return mission (refs. 3 and 6). The aerocapture missions under present consideration are the Mars Surface Sample Return (MSSR), Saturn Orbiter Dual Probe (SO2P), and Titan Orbiter (TO) missions.

The aerocapture mission is possible for any planet (or satellite) which has an atmosphere. The aerocapture technique begins with the interplanetary cruise vehicle (aerocapture vehicle) approaching the reference body (planet or satellite) on a hyperbolic trajectory and removing its excess energy in a single pass through the atmosphere to achieve the initial required orbit about the celestial body. As such, a aerocapture is a system concept that

utilizes aerodynamic drag to acquire the velocity depletion necessary to obtain a closed planetary orbit from a hyperbolic flyby trajectory. It is accomplished through a aerodynamically controlled atmospheric entry during which the vehicle's in-plane lift-to-drag ratio is varied to maintain a constant drag. The aerocapture offers significant gains in payload and choice of orbits, and eliminates fuel-costly retro-propulsion module (RPM) for planetary orbiter missions (ref. 4).

For missions to outer planets, use of the aerocapture concept in a convenient atmosphere-bearing satellite of the target planet has been emphasized. Thus, it has been proposed to use the atmosphere of Titan for braking into a Saturn orbit. The use of Titan's atmosphere would minimize the entry speed requirement for aerocapture, and this, in turn, would minimize the thermal protection requirements of the aerocapture vehicle. The Titan's aerocapture concept (for Saturn orbital mission) is expected to cut the interplanetary cruise travel time to Saturn from 8 to 3.5 years. A Titan orbiter mission using anything other than aerocapture is presently impossible (ref. 4). For Titan's aerocapture mission, the need for high performance entry vehicle geometrics and high performance thermal protection systems has been stressed (refs. 4 and 5). In partial support of this need, it is essential to provide a complete analysis of aerothermodynamic environment of the Titan aerocapture vehicle.

The main objective of this study, therefore, is to determine the extent of convective and radiative heating to the aerocapture vehicle under different entry conditions. This essentially can be accomplished by assessing the heating rates in the stagnation and windward regions of an equivalent body. The equivalent body configuration considered for this study is a 45° sphere cone at zero angle of attack. Different compositions for the Titan's $N_2 - CH_4$ atmosphere have been assumed and results have been obtained for various entry trajectories suggested by the Jet Propulsion Laboratory (JPL).

BASIC FORMULATION

The physical model and coordinate system considered for the equivalent body are shown in Figure 1(a,b). The hypersonic flow of radiating and reacting gas mixture in the shock layer is assumed to be axisymmetric, steady,

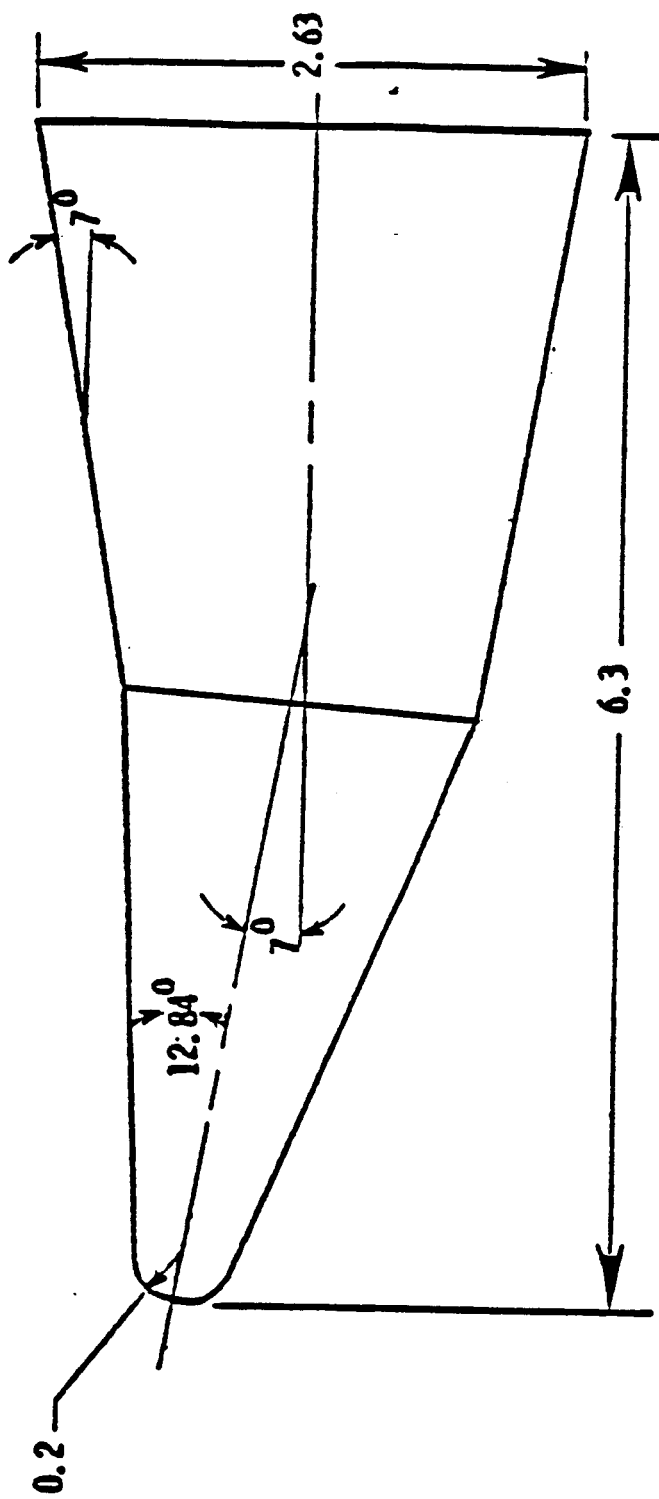


Figure 1(a). Titan aerocapture vehicle configuration.

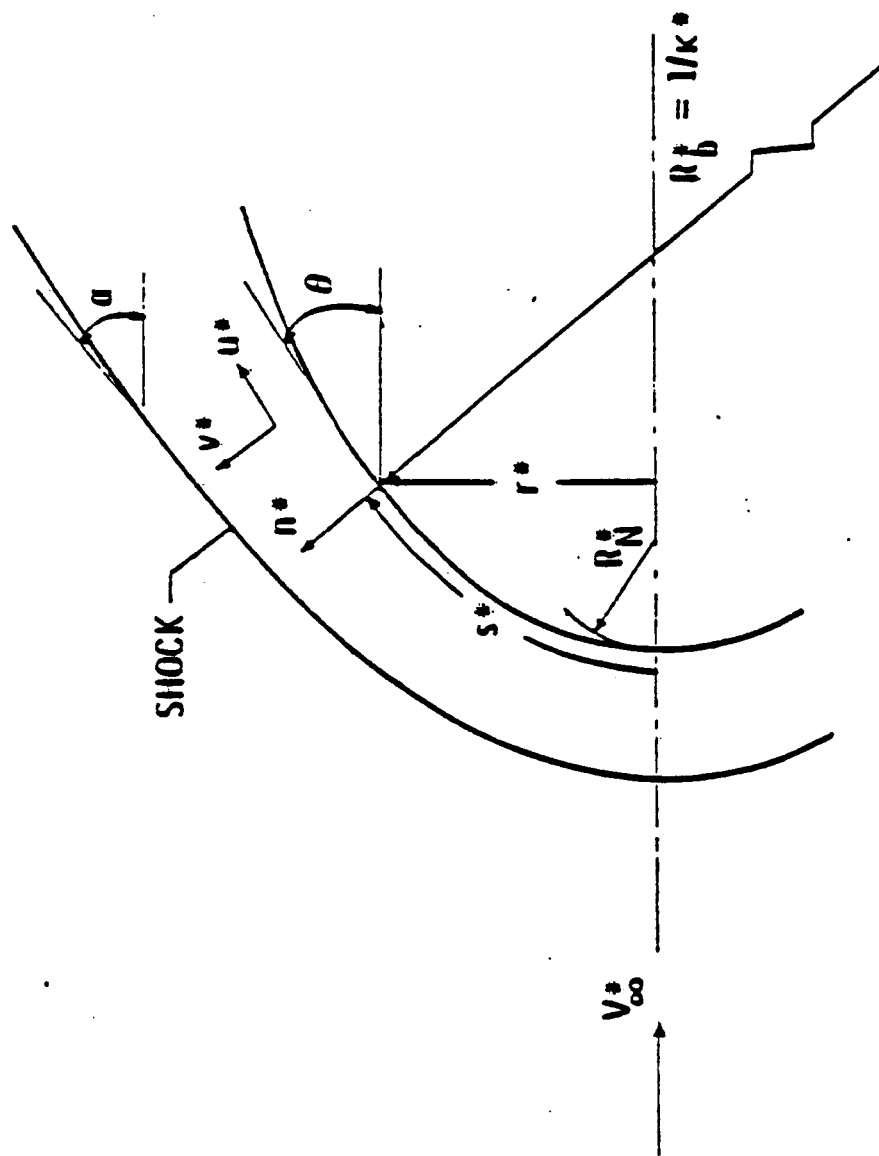


Figure 1(b). Coordinate system.

viscous, and in chemical and local thermodynamic equilibrium. Basic governing equations for this physical model are available in the literature (refs. 7-9). The nondimensional form of the viscous shock-layer equations that are applicable in the present case can be expressed as (refs. 10 and 11):

Continuity:

$$\left(\frac{\partial}{\partial s}\right)(\zeta\rho\mu) + \left(\frac{\partial}{\partial n}\right)(\Gamma\zeta\rho v) = 0 \quad (1)$$

s-momentum:

$$\begin{aligned} \rho \left[\left(\frac{u}{\Gamma}\right) \left(\frac{\partial u}{\partial s}\right) + u \left(\frac{\partial u}{\partial n}\right) + \frac{uv\kappa}{\Gamma} \right] + \Gamma^{-1} \left(\frac{\partial p}{\partial s}\right) \\ = \epsilon^2 \left[\left(\frac{\partial}{\partial n}\right)(\mu\psi) + \mu \left(\frac{2\kappa}{\Gamma} + \frac{\cos \theta}{\zeta}\right) + \psi \right] \end{aligned} \quad (2)$$

n-momentum:

$$\rho \left[\left(\frac{u}{\Gamma}\right) \left(\frac{\partial v}{\partial s}\right) + u \frac{\partial v}{\partial n} - \frac{u^2\kappa}{\Gamma} \right] + \frac{\partial p}{\partial n} = 0 \quad (3)$$

Energy:

$$\begin{aligned} \rho \left[\left(\frac{u}{\Gamma}\right) \left(\frac{\partial H}{\partial s}\right) + v \left(\frac{\partial H}{\partial n}\right) \right] - v \left(\frac{\partial p}{\partial n}\right) + \frac{\rho\kappa u^2 v}{\Gamma} \\ = \epsilon^2 \left[\frac{\partial \phi}{\partial n} + \left(\frac{\kappa}{\Gamma} + \frac{\cos \theta}{\zeta}\right) \phi \right] - \text{div } q_r \end{aligned} \quad (4)$$

Elemental continuity:

$$\rho \left[\left(\frac{u}{\Gamma}\right) \left(\frac{\partial \tilde{C}_l}{\partial s}\right) + v \left(\frac{\partial \tilde{C}_l}{\partial n}\right) \right] = \left\{ \left(\frac{\partial}{\partial n}\right) \left[\left(\frac{\Gamma\zeta\mu Le}{Pr}\right) \left(\frac{\partial \tilde{C}_l}{\partial n}\right) \right] \right\} \quad (5)$$

State:

$$p = \frac{\rho^* T R^*}{M^* C_{p,\infty}^*} \quad (6)$$

where

$$\Gamma = 1 + n\kappa, \quad \zeta = r + n \cos \theta \quad (7a)$$

$$\epsilon = \frac{\mu_{\text{ref}}^*}{\rho_{\infty}^* V_{\infty}^* R_N^*}^{1/2} \quad (7b)$$

$$\psi = \frac{\partial u}{\partial n} - \frac{u\kappa}{\Gamma} \quad (7c)$$

$$\begin{aligned} \phi = & \frac{\mu}{Pr} \frac{\partial H}{\partial n} + (Le - 1) \sum_{i=1}^N h_i \frac{\partial C_i}{\partial n} \\ & + (Pr - 1) u \frac{\partial u}{\partial n} - Pr \kappa \frac{u^2}{\Gamma} \end{aligned} \quad (7d)$$

$$H = h + \frac{u^2}{2}, \quad \tilde{C}_{\ell} = \sum_{i=1}^N \delta_{i\ell} \frac{M_{\ell}^*}{M_i^*} C_i. \quad (7e)$$

In equation (5), \tilde{C}_{ℓ} is the mass fraction of element ℓ ; and in the definition of \tilde{C}_{ℓ} , $\delta_{i\ell}$ represents the number of atoms of the ℓ th element in species i .

The set of governing equations presented has a hyperbolic-parabolic nature. The hyperbolic nature enters through the normal momentum equation. If the shock layer is assumed thin, then the normal momentum equation can be expressed as

$$\frac{\rho u^2 \kappa}{(1 + n\kappa)} = \frac{\partial p}{\partial n} \quad (8)$$

If equation (3) is replaced with equation (8), then the resulting set of equations is parabolic. These equations can, therefore, be solved by using numerical procedures similar to those used in solving boundary-layer problems (refs. 8 and 12).

In order to solve the preceding set of governing equations, it is essential to specify appropriate boundary conditions at the body surface and at the shock. At the body surface (wall), no-slip and no temperature jump conditions are used. Consequently, $u_w = v_w = 0$, and the wall temperature is either specified or calculated. The conditions in front of the shock are obtained from the freestream entry conditions. The conditions immediately behind the shock are obtained by using the Rankine-Hugoniot relations (refs. 8 and 9).

The heat transferred to the wall due to conduction and diffusion is referred to here as the convective heat flux and is given by the relation

$$q_{c,w} = -\epsilon^2 k \frac{\partial T}{\partial n} + \frac{\mu Le}{Pr} \sum_{i=1}^N \frac{\partial C_i}{\partial n} h_{i,w} \quad (9)$$

The convective heat transfer is often described by a dimensionless parameter called Stanton number. For the viscous-shock-layer flow, the Stanton number is given by

$$St = \frac{q_{c,w}}{(H_\infty - H_w)} \quad (10)$$

The governing equations and boundary conditions presented here essentially describe the flowfield in the shock layer. It now remains to specify the equilibrium gas composition and obtain appropriate relations for the radiative flux and thermodynamic and transport properties.

Equilibrium Gas Composition

Analyses of chemically reacting flows are usually simplified by assuming the chemical equilibrium behavior of the gas mixture. The equilibrium chemical reactions considered for this study are confined to a system of carbon, hydrogen, and nitrogen. The Aerotherm Chemical Equilibrium (ACE)

computer program was used to determine various chemical species under different pressure and temperature conditions and for different freestream atmospheric compositions. Further information on equilibrium gas composition and freestream atmospheric conditions is given in the next section dealing with physical conditions and data source.

Radiation Transport Model

The tangent slab approximation for radiative transfer is used in this study. This implies that the radiative energy transfer along the body is negligible in comparison to that transferred in the direction normal to the body. It should be noted that the tangent slab approximation is used only for the radiative transport and not for other flow variables. For nonscattering boundary surfaces, a one-dimensional expression for the net radiation flux in the shock layer is given by (refs. 9 and 13)

$$q_r = q_r^+ - q_r^- \quad (11)$$

where q_r^+ represents the energy transfer toward the shock and q_r^- the energy transfer toward the body. The expressions for q_r^+ and q_r^- are available in the cited references.

The radiative flux, q_r , is calculated with the radiative transport code RAD (ref. 14) which accounts for detailed nongray radiation absorption and emission processes. The chemical species considered for determining the radiative transport are N, N₂, N⁺, N⁻, N₂⁺, H, H₂, H⁻, e⁻, C, C⁻, C⁺, and CN.

PHYSICAL CONDITIONS AND DATA SOURCE

As pointed out earlier, the entry body considered for this study is a 45°-sphere cone at a zero-degree angle of attack (fig. 1). The body temperature is assumed to be 2,000 K and, for most cases, the body nose radius is taken to be 0.2 m.

Entry Trajectory and Freestream Conditions

As discussed in reference 4, a nominal aerocapture mission has two critical phases, approach navigation and atmospheric flight. Approach trajectory correction maneuvers outside the atmosphere can be controlled by commands computed on Earth. However, once the vehicle enters the atmosphere, trajectory maneuvers must be computed and commanded on board. For the Titan aerocapture mission, entry trajectories have been generated by the Jet Propulsion Laboratory. The altitude history for an aerocapture vehicle is illustrated in figure 2 for two different (shallow and steep) entry angles. The entry trajectories and freestream conditions used in this study are given in tables 1 to 5.

Chemical Composition of Gas Mixture

At the initiation of this study, the atmospheric conditions of Titan were not defined clearly. As such, different atmospheric compositions were assumed for a parametric study. Now, it is evident that Titan, the largest moon in the solar system, is wrapped essentially in a dense atmosphere of nitrogen vapors (rather than methane, the best guess before Voyager 1) (ref. 15). Thus, a realistic case would be to assume a very high concentration of nitrogen in the freestream gas mixture. However, to study the effect of freestream gas composition on heating of the entry vehicle, different gas compositions were assumed.

The equilibrium composition is determined by a free energy minimization calculation as developed in reference 16. As mentioned earlier, the Aero-therm Chemical Equilibrium computer program was used to determine various chemical species for different pressure, temperature, and freestream conditions. For initial study, 68 chemical species for carbon-hydrogen-nitrogen system were included in the matrix of calculations for a given freestream atmospheric composition. The matrix was

Pressure: 0.1, 0.5, 1.0, and 5 atm

Temperature: 2,000 K to 10,000 K in 500 K increments

Composition: 99.5% N₂ + 0.5% CH₄, 90% N₂ + 10% CH₄,
75% N₂ + 25% CH₄, 50% N₂ + 50% CH₄,
25% N₂ + 75% CH₄, 10% N₂ + 90% CH₄

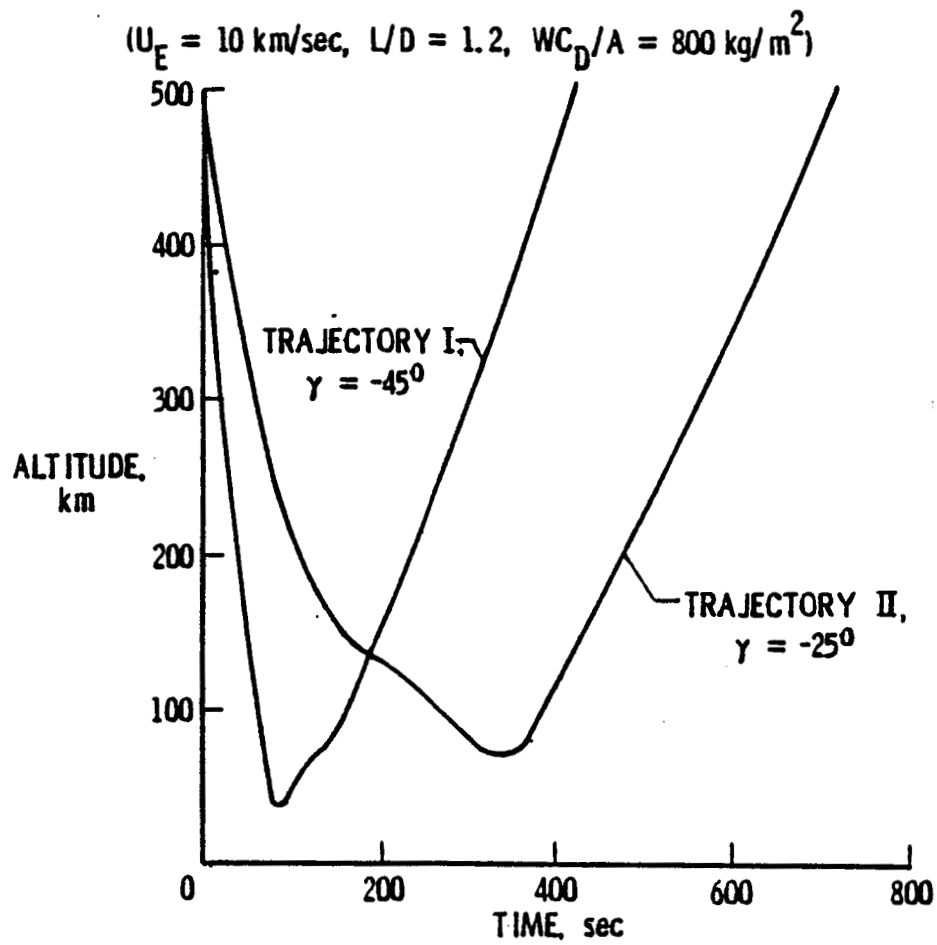


Figure 2. The altitude history for an aerocapture vehicle.

Table 1. Altitude and freestream conditions: Trajectory I
(L/D = 1.2, $\gamma = -45^\circ$, $\beta = 800 \text{ kg/m}^2$, $U_E = 10 \text{ km/s}$).

TIME (s)	ALTITUDE (km)	ρ_∞ (g/cm ³)	ρ_∞ (mb)	T_∞ (K)	V_∞ (km/s)	MACH NO.
40	230.965	0.1265E-6	0.10355	159.10	9.929	29.13
50	169.824	0.3473E-6	0.24562	139.44	9.803	30.72
60	114.238	0.1022E-5	0.64627	119.17	9.431	31.90
70	70.409	0.3197E-5	1.5836	103.16	8.448	30.78
78	50.922	0.5157E-5	2.5901	96.28	7.185	27.10
90	48.539	0.5512E-5	2.7449	95.56	5.502	20.83
100	60.654	0.3944E-5	1.9738	99.26	4.727	17.56
150	95.613	0.1604E-5	0.89555	112.46	3.406	11.89
220	173.831	0.3728E-6	0.23159	140.84	3.015	9.40

Table 2. Altitude and freestream conditions: Trajectory II
($L/D = 1.2$, $\gamma = -25^\circ$, $\beta = 800 \text{ kg/m}^2$, $U_E = 10 \text{ km/s}$).

TIME (s)	ALTITUDE (km)	ρ_∞ (g/cm ³)	ρ_∞ (mb)	T_∞ (K)	V_∞ (km/s)	MACH NO.
50	321.264	0.3952E-7	0.3249E-1	160.00	9.953	29.11
100	213.217	0.1654E-6	0.1335E+0	155.60	9.689	28.74
110	198.471	0.2063E-6	0.1638E+0	150.30	9.583	28.91
120	185.306	0.2694E-6	0.1967E+0	145.10	9.451	29.03
130	173.617	0.3288E-6	0.2323E+0	140.76	9.286	28.96
140	163.335	0.3812E-6	0.2683E+0	137.16	9.100	28.75
150	154.339	0.4687E-6	0.3139E+0	134.02	8.889	28.41
170	141.502	0.6712E-6	0.3909E+0	129.53	8.358	27.18
175	139.412	0.7052E-6	0.4053E+0	128.79	8.210	26.77
180	137.610	0.7213E-6	0.4215E+0	128.16	8.062	26.36
200	130.832	0.7855E-6	0.4875E+0	125.79	7.495	24.73

Table 3. Altitude and freestream conditions: Trajectory III
 $(L/D = 1.2, \gamma = -45^\circ, \beta = 800 \text{ kg/m}^2, U_E = 6 \text{ km/s})$.

TIME (s)	ALTITUDE (km)	ρ_∞ (g/cm ³)	ρ_∞ (mb)	T_∞ (K)	V_∞ (km/s)	MACH NO.
90	144.674	0.6142E-6	0.3719	130.00	5.847	18.93
100	111.891	0.1076E-5	0.6732	118.70	5.681	19.29
110	83.284	0.2349E-5	1.1359	108.10	5.379	19.14
120	61.655	0.3859E-5	1.9338	99.60	4.872	18.06
129	49.822	0.5318E-5	2.6615	95.90	4.327	16.35
140	45.041	0.6079E-5	2.9723	94.50	3.690	14.04
150	47.699	0.5643E-5	2.7995	95.30	3.245	12.30
160	54.496	0.4666E-5	2.3577	97.30	2.934	11.01
170	63.709	0.3693E-5	1.8516	100.50	2.724	10.05

Table 4. Altitude and freestream conditions: Trajectory IV
(L/D = 1.2, $\gamma = -45^\circ$, $\beta = 800 \text{ kg/m}^2$, $U_E = 8 \text{ km/s}$).

TIME (s)	ALTITUDE (km)	ρ_∞ (g/cm ³)	ρ_∞ (mb)	T_∞ (K)	V_∞ (km/s)	MACH NO.
60	181.218	0.2927E-6	0.2070	143.48	7.883	24.35
70	134.830	0.7469E-6	0.4464	127.19	7.709	25.30
80	93.931	0.1689E-5	0.9283	111.87	7.329	25.63
90	63.296	0.3726E-5	1.868	100.32	6.515	24.07
97	50.882	0.5162E-5	2.592	96.26	5.783	21.81
110	46.913	0.5768E-5	2.850	95.07	4.554	17.28
120	54.841	0.4621E-5	2.335	97.17	3.961	14.84
130	67.354	0.3413E-5	1.706	101.94	3.603	13.20
150	98.351	0.1473E-5	0.8421	113.42	3.240	11.25

Table 5. Altitude and freestream conditions: Trajectory V
(L/D = 1.2, $\gamma = -45^\circ$, $\beta = 800 \text{ kg/m}^2$, $U_E = 13\text{km/s}$).

TIME (s)	ALTITUDE (km)	ρ_∞ (g/cm ³)	ρ_∞ (mb)	T_∞ (K)	V_∞ (km/s)	MACH NO.
30	237.512	0.1143E-6	0.0937	159.75	12.905	37.77
40	158.551	0.4165E-6	0.2887	135.49	12.672	40.28
50	90.769	0.1863E-5	0.9899	110.77	11.777	41.40
60	51.374	0.5092E-5	2.560	96.41	9.361	35.28
61	49.676	0.5339E-5	2.671	95.90	9.084	34.33
70	49.557	0.5357E-5	2.678	95.86	7.047	26.64
80	67.533	0.3401E-5	1.698	102.01	5.912	21.66
100	101.803	0.1345E-5	0.7892	114.72	5.083	17.56
120	124.659	0.8488E-6	0.5381	123.63	4.762	15.84

For a freestream gas composition of 90% N_2 + 10% CH_4 , the variation in mole fraction of different species, as a function of temperature, is illustrated in figure 3 for $P = 1$ atm. For this case, there are 21 chemical species in the gas mixture. However, concentration of some species is less than 0.05% for the range of temperature considered. Similar trends were noted for other pressures and freestream gas compositions (ref. 17). For this study, therefore, contributions of at least 18 chemical species (N_2 , N , N^+ , C_3 , C_2 , C , C^+ , CH_4 , C_3H , C_2H_2 , C_2H , C_2N , CN , H_2 , H , H^+ , HCN , and e^-) were considered for the shock-layer gas mixture.

Thermodynamic and Transport Properties

Thermodynamic properties for specific heat, enthalpy, and free energy, and transport properties for viscosity and thermal conductivity are required for each species considered in the shock-layer gas. Values for the thermodynamic (refs. 18 and 19) and transport (ref. 20) properties are obtained by using polynomial curve fits. The mixture viscosity is obtained by using the semiempirical formulae of Wilke (ref. 7). In this study, the Lewis and Prandtl numbers are taken to be 1.1 and 0.64 respectively (ref. 21).

METHOD OF SOLUTION

Davis (ref. 12) presented a method for solving the viscous-shock-layer equations for stagnation and downstream flow. Mass (ref. 8) and Tiwari and Szema (ref. 9) applied this method of solution to reacting multicomponent mixtures. The entire solution procedure is discussed in detail in references 8 and 9.

RESULTS AND DISCUSSION

Results have been obtained for entry conditions given in tables 1 to 5 to investigate the effects of freestream gas composition, entry velocity, and body nose radius on the stagnation-point convective and radiative heating. Specific results were obtained to determine the extent of convective and radiative heating along the body for freestream gas composition of 90% N_2 + 10% CH_4 and 99.5% N_2 + 0.5% CH_4 . Selected results for Trajectories I and II are given in tables 6 and 7 and extensive tabulations of all results

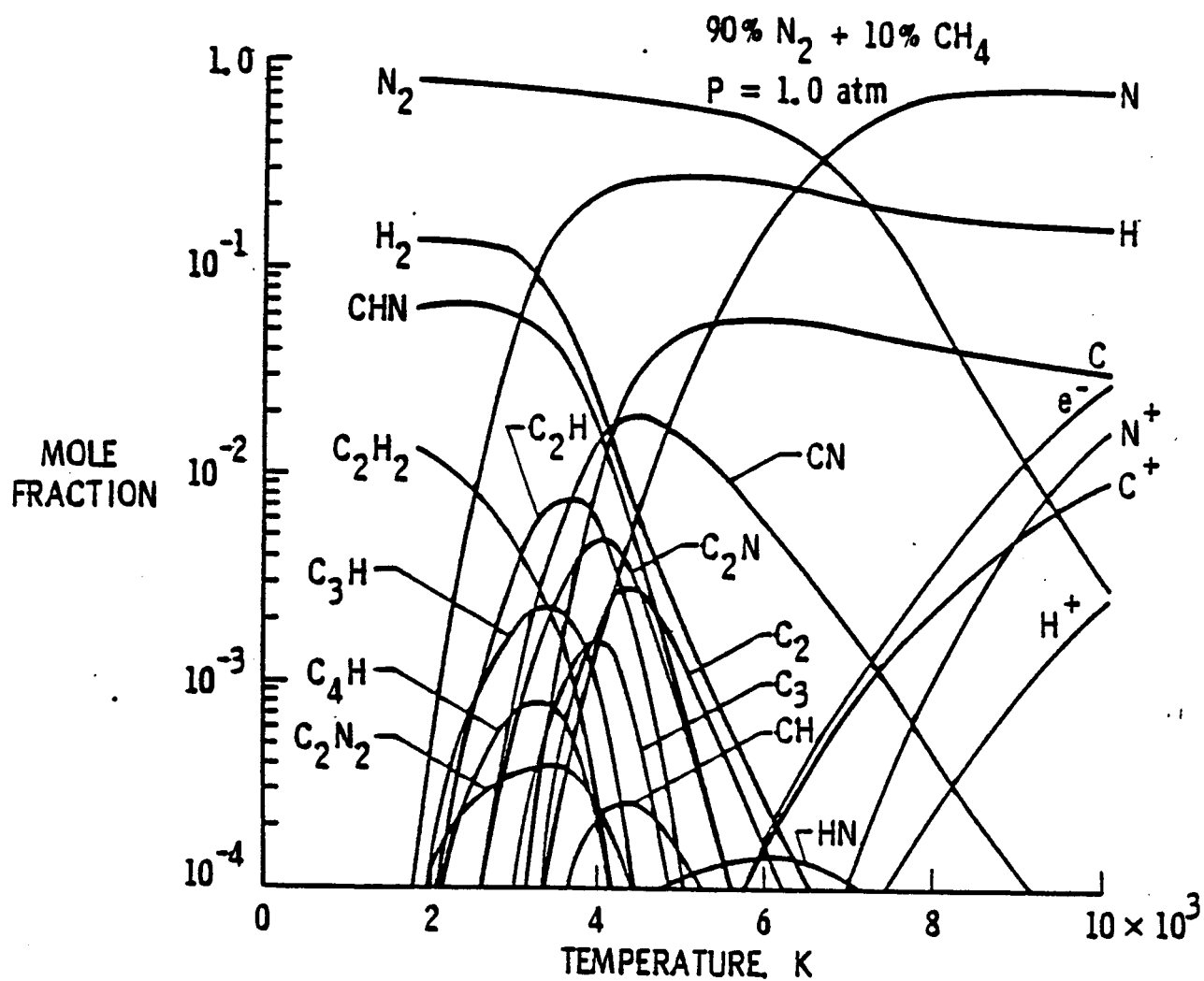


Figure 3. Variation in mole fraction of different species for P = 1.0 atm and 90% N₂ + 10% CH₄.

Table 6. Stagnation results (sphere cone, $R_N = 0.2$ m, $T_w = 2,000$ K):
atmosphere - 99.5% N_2 + 0.5% CH_4 , Trajectory I.

(a)

TIME (s)	ρ_∞ (kg/m ³)	P_s (atm)	ρ_s/ρ_∞	T_s (K)	n_s (cm)	$q_{c,w}$ (MW/m ²)	$q_{r,w}$ (MW/m ²)
40	0.1265E-3	0.1163	18.13	8508	0.7963	5.783	0.0044
50	0.3473E-3	0.3112	17.93	8498	0.8241	8.558	0.0155
60	0.1022E-2	0.8473	17.76	8262	0.8381	12.265	0.0576
70	0.3197E-2	2.1194	16.75	7902	0.8927	14.818	0.2391
78	0.5157E-2	2.4560	15.08	7354	1.0011	11.188	0.3136
90	0.5512E-2	1.5121	12.10	6412	1.2341	4.688	0.2249
100	0.3944E-2	0.7888	10.48	5813	1.4109	2.290	0.1387

Table 6. (Concluded.)

(b)

TIME (s)	h_w (kJ/kg)	h_s (kJ/kg)	St	Re
40	2.045E+03	48.799E+03	0.9797E-01	0.1065E+04
50	2.045E+03	47.629E+03	0.5497E-01	0.2867E+04
60	2.045E+03	44.082E+03	0.3013E-01	0.8317E+04
70	2.045E+03	35.275E+03	0.1640E-01	0.2488E+05
78	2.045E+03	25.445E+03	0.1280E-01	0.3783E+05
90	2.045E+03	14.799E+03	0.1200E-01	0.3679E+05
100	2.045E+03	10.873E+03	0.1374E-01	0.2513E+05

Table 7. Stagnation results (sphere cone, $R_N = 0.2$ m, $T_w = 2,000$ K):
atmosphere - 90% N_2 + 10% CH_4 .

(a)

TIME (s)	ρ_∞ (kg/m ³)	P_s (atm)	ρ_s/ρ_∞	T_s (K)	n_s (cm)	$q_{c,w}$ (MW/m ²)	$q_{r,w}$ (MW/m ²)
<u>Atmosphere - 90% N_2 + 10% CH_4, Trajectory I</u>							
40	0.1265E-3	0.1165	18.56	7259	0.8029	5.247	0.0177
50	0.3473E-3	0.3112	17.95	7460	0.8440	8.126	0.0713
60	0.1022E-2	0.8455	17.15	7544	0.8880	11.637	0.3569
70	0.3197E-2	2.1108	15.74	7342	0.9619	13.498	2.0398
78	0.5157E-2	2.443	14.08	6733	1.0642	9.687	3.7697
90	0.5512E-2	1.512	12.10	5269	1.2120	3.543	3.8894
100	0.3944E-2	0.7999	12.10	4127	1.2208	1.683	1.5915
<u>Atmosphere - 90% N_2 + 10% CH_4, Trajectory II</u>							
140	0.3812E-3	0.2942	17.78	6953	0.8586	6.437	0.0862
150	0.4687E-3	0.3449	17.49	6895	0.8731	6.523	0.1190
170	0.6712E-3	0.4355	16.75	6729	0.9111	6.242	0.2044
175	0.7052E-3	0.4413	16.58	6665	0.9201	6.061	0.2206
180	0.7213E-3	0.4350	16.39	6596	0.9300	5.747	0.2287
200	0.7855E-3	0.4081	15.63	6330	1.9723	4.589	0.2728

Table 7. (Concluded.)

(b)

TIME (s)	h_w (kJ/kg)	h_s (kJ/kg)	St	Re
<u>Atmosphere - 90% N₂ + 10% CH₄, Trajectory I</u>				
40	2.877E+03	48.397E+03	0.9140E-01	0.1221E+04
50	2.877E+03	47.175E+03	0.5365E-01	0.3250E+04
60	2.877E+03	43.595E+03	0.2949E-01	0.9229E+04
70	2.877E+03	38.804E+03	0.1554E-01	0.2736E+05
78	2.877E+03	25.002E+03	0.1173E-01	0.4218E+05
90	2.877E+03	14.347E+03	0.1007E-01	0.4460E+05
100	2.877E+03	10.440E+03	0.1182E-01	0.3408E+05
<u>Atmosphere - 90% N₂ + 10% CH₄, Trajectory II</u>				
140	2.877E+03	40.565E+03	0.4904E-01	0.3576E+04
150	2.877E+03	38.609E+03	0.4352E-01	0.4358E+04
170	2.877E+03	34.094E+03	0.3545E-01	0.6097E+04
175	2.877E+03	32.835E+03	0.3470E-01	0.6378E+04
180	2.877E+03	31.651E+03	0.3411E-01	0.6494E+04
200	2.877E+03	27.239E+03	0.3175E-01	0.6941E+04

are available in reference 17. Some specific results of the study are presented in this section. It should be noted that, for clarity, the asterisks on the dimensional quantities have been left out from the tables and figures.

The effects of freestream gas composition on the shock temperature are illustrated in figures 4 and 5. The results show that the shock temperature (as well as the temperature in the shock layer, fig. 5) increases with increasing N_2 concentration. This is because N_2 provides less energy accommodation in comparison to CH_4 . The stagnation shock temperatures are relatively higher for early entry times (fig. 4); this, however, would be expected because of relatively higher freestream velocities. The results of figure 5 show that the temperature gradient in the shock layer is restricted essentially in the regions near the body surface for all freestream gas compositions.

The effects of gas composition on the stagnation-point convective and radiative heating are illustrated in figures 6-8. The convective heating is seen to increase with increasing N_2 concentration (fig. 6) with peak heating occurring at about 70 sec. This is a direct consequence of the variation in the shock temperature. The situation, however, is not the same with respect to the radiative heating (fig. 7), i.e., the radiative heating does not necessarily increase with increasing N_2 concentration. This is because, for a given set of conditions, the radiative transfer strongly depends on the presence of absorbing-emitting species in the gas mixture. It is also evident from figure 7 that the peak radiative heating occurs at different times for different freestream gas compositions. For N_2 concentrations higher than 75%, the peak radiative heating is seen to occur at about 78 sec. Furthermore, the results show that the radiative heating would be significant only for N_2 concentrations between 50% and 90%; the maximum heating is noted for 75% N_2 concentration. For the freestream composition of 99.5% N_2 + 0.5% CH_4 (which is considered to be a realistic composition for the Titan's atmosphere), the results for stagnation-point shock temperature and convective and radiative heating are illustrated in figure 8 for Trajectory I. It is noted that, for this case, the radiative heating is negligible as compared to the convective heating.

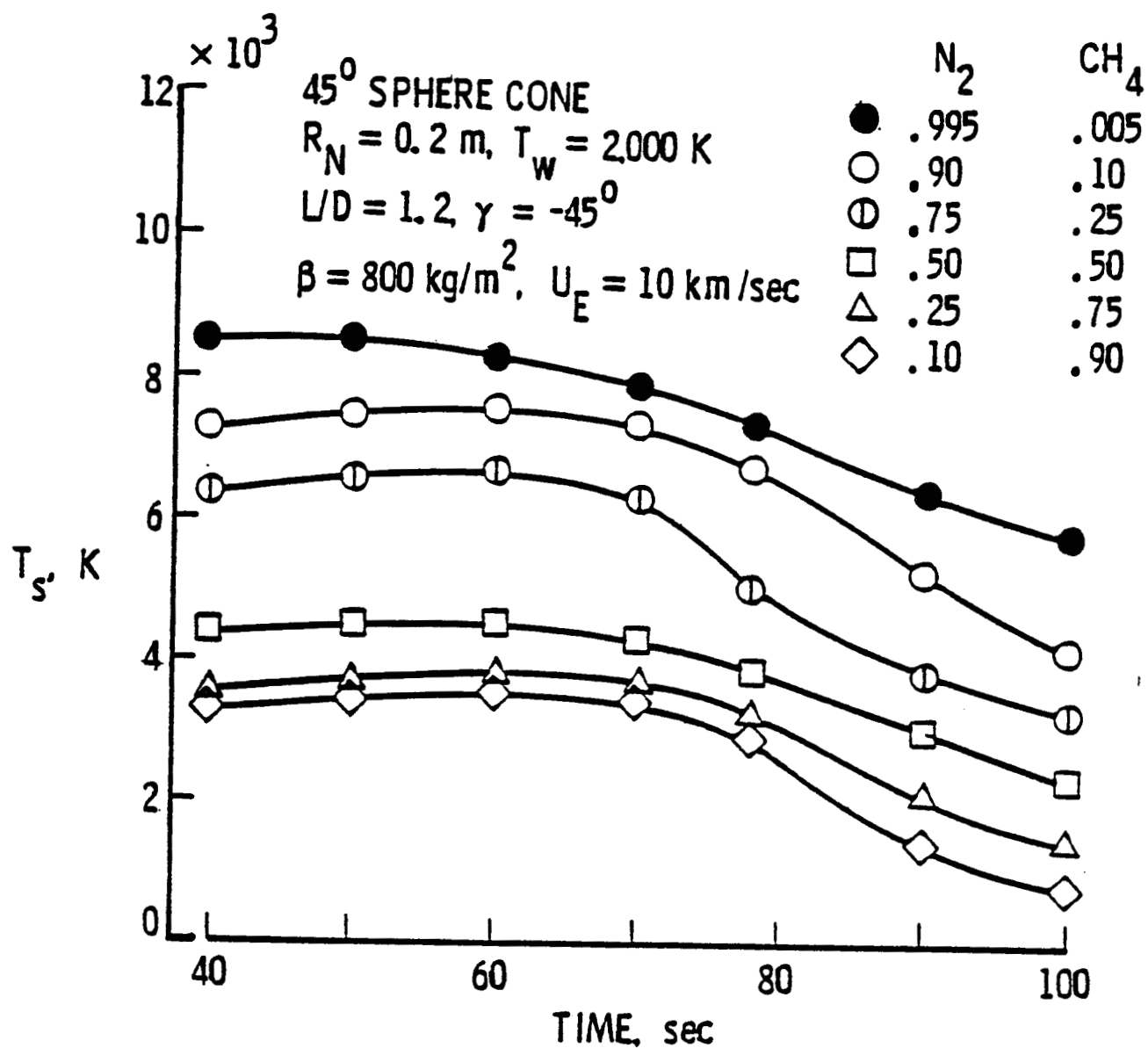


Figure 4. Effect of gas composition on stagnation-point shock temperature, Trajectory I.

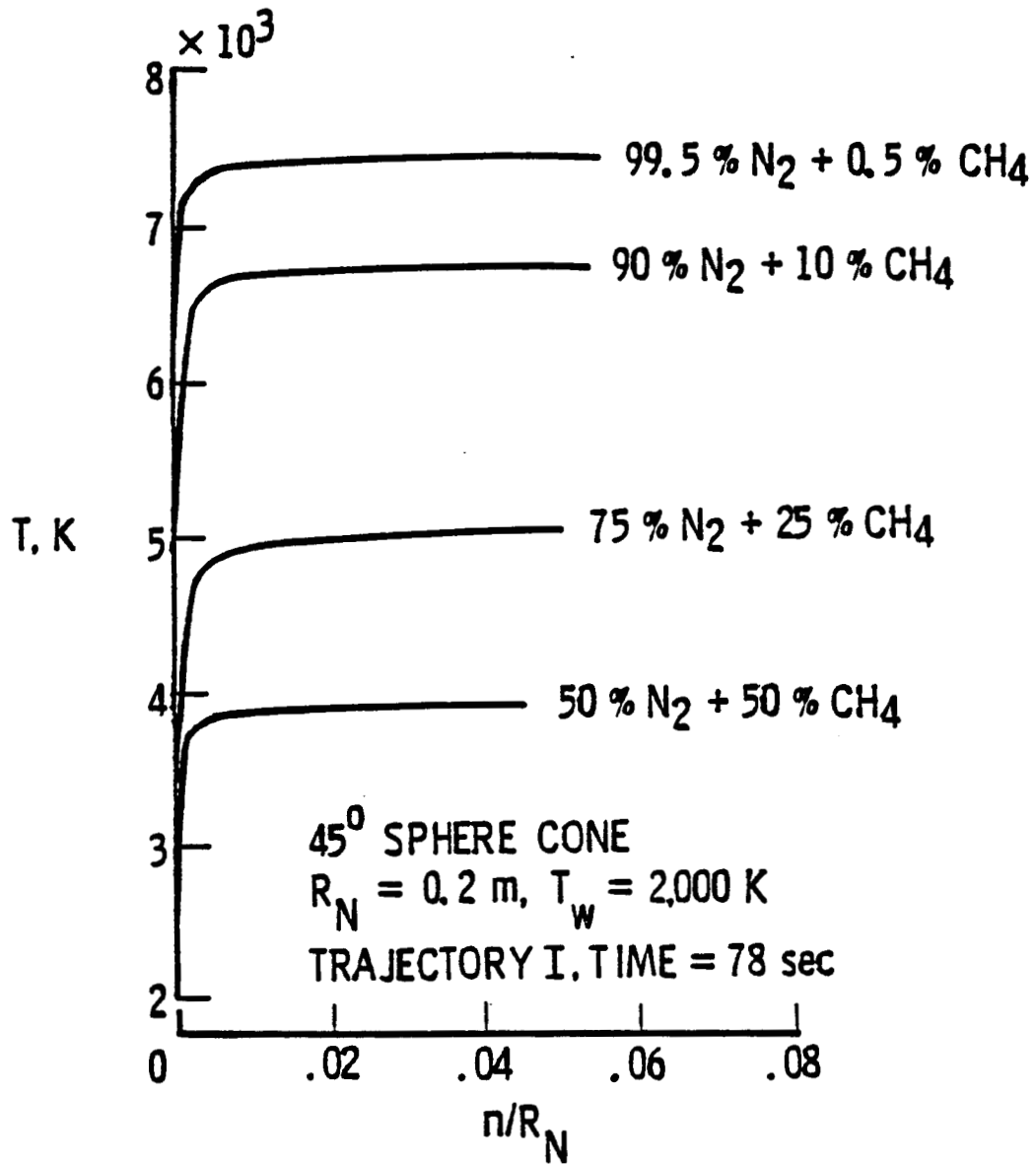


Figure 5. Effect of gas composition on temperature distribution along the stagnation streamline, Trajectory I (time = 78 s).

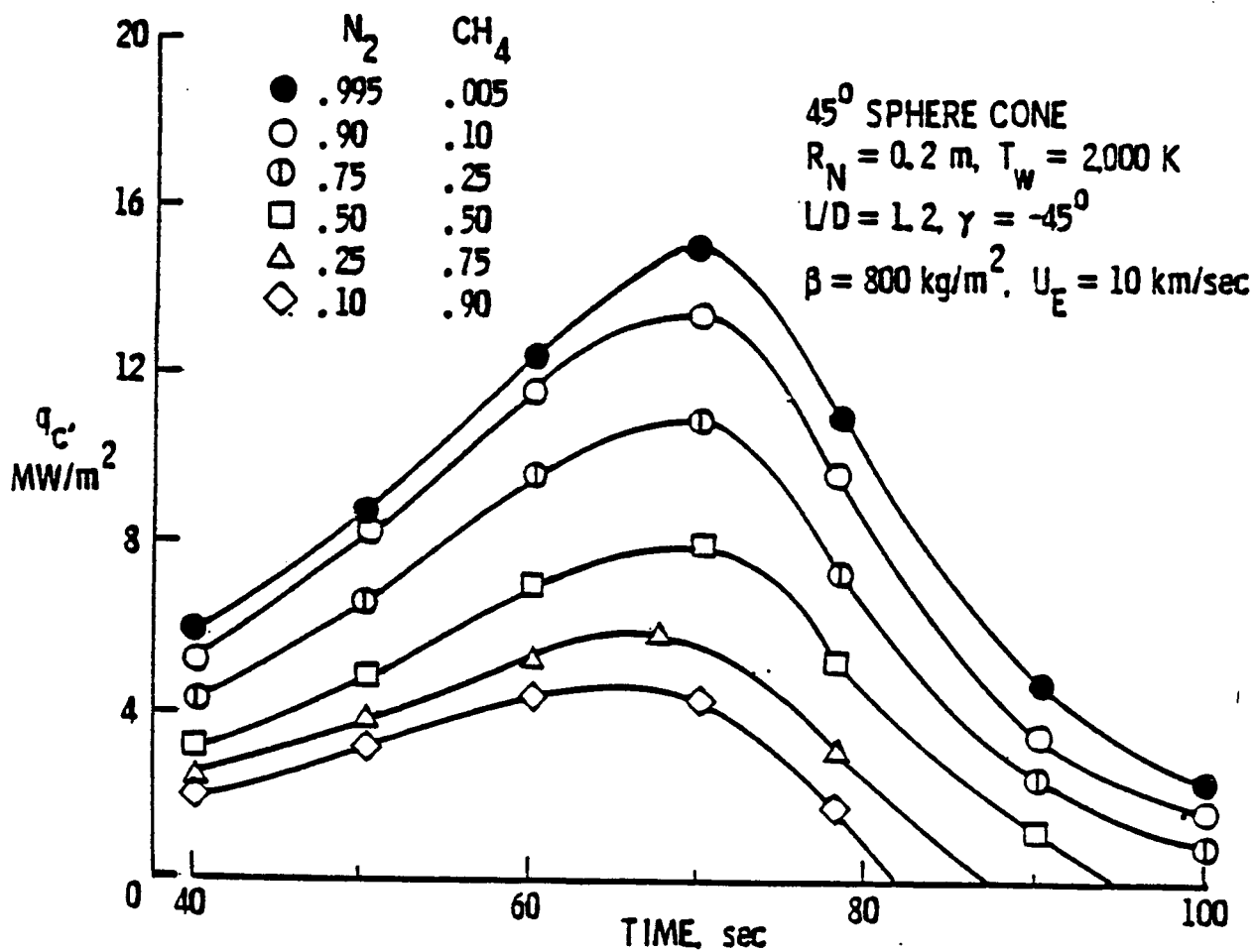


Figure 6. Effect of gas composition on stagnation-point convective heating, Trajectory I.

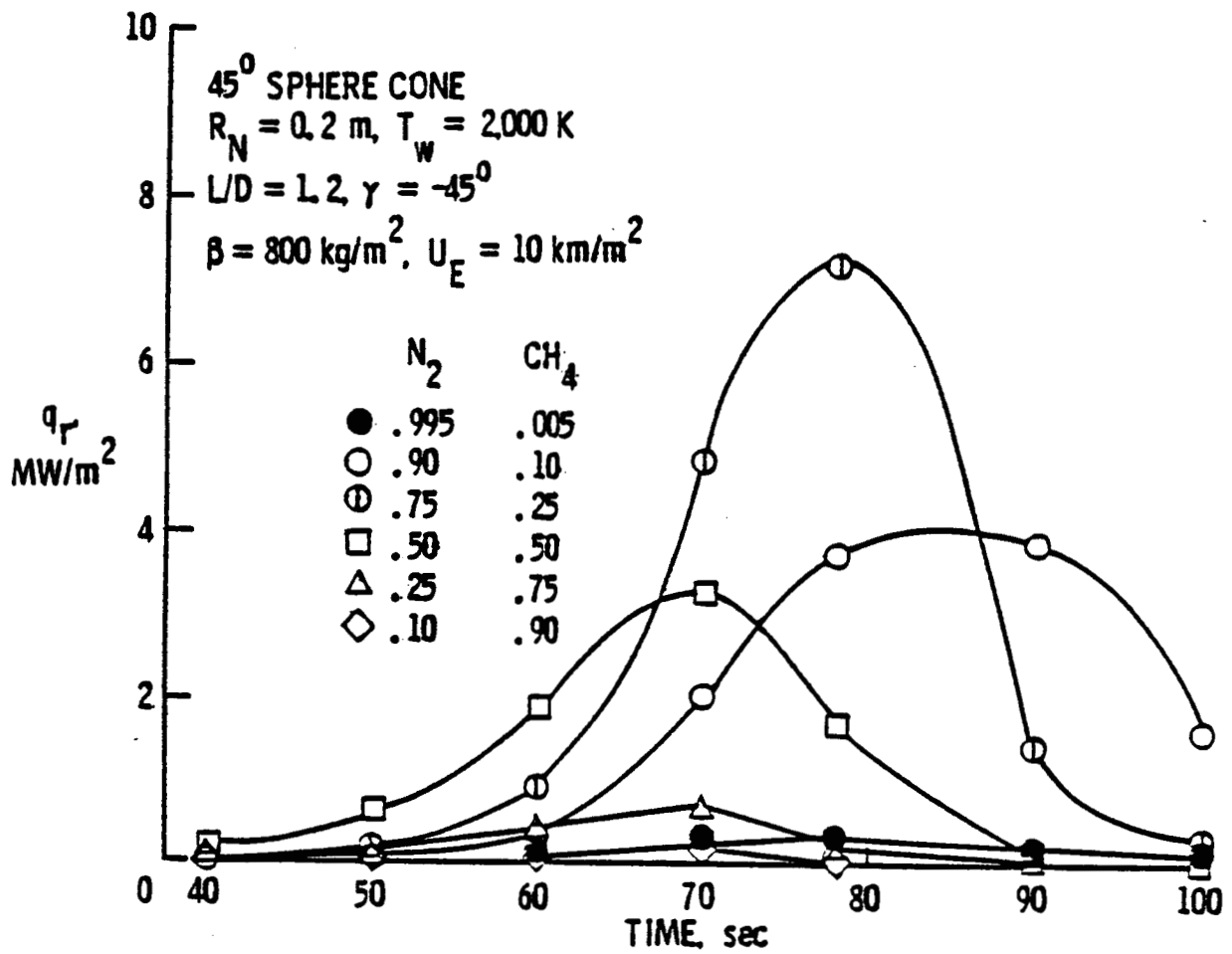


Figure 7. Effect of gas composition on stagnation-point radiative heating.

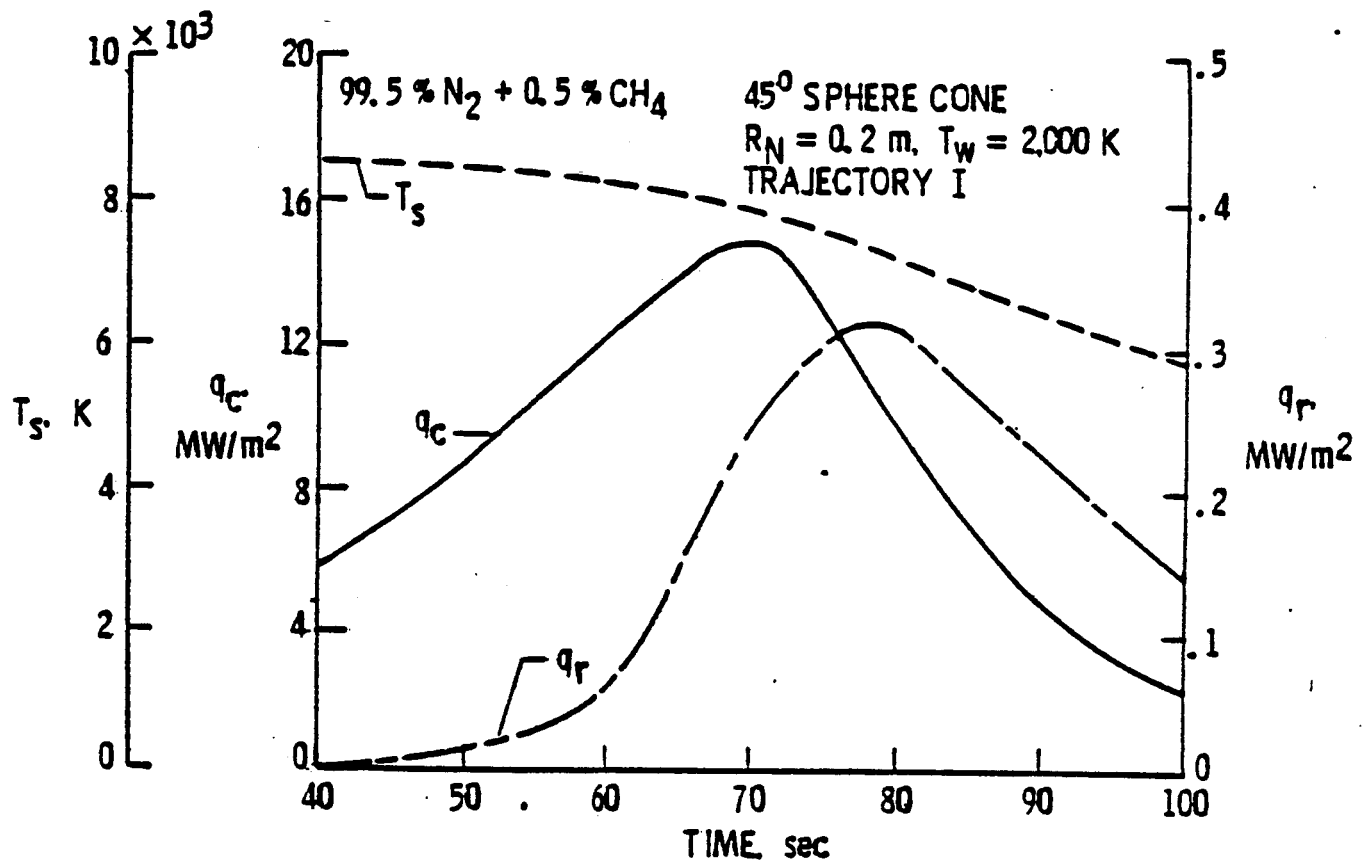


Figure 8. Variation of stagnation-point shock temperature and convective and radiative heating for 99.5% N_2 + 0.5% CH_4 .

The effects of entry velocity on the stagnation-point shock temperature and convective and radiative heating rates are illustrated in figures 9-11(a). For the freestream gas composition of 90% N_2 + 10% CH_4 , the results presented in figures 9-11(a) show that the shock temperature and heating rates, in general, increase with increasing entry velocity for a fixed entry altitude (time). It is seen that the extent of convective heating is considerably higher than the radiative heating for all cases. As noted earlier, the convective and radiative heating peaks occur at different entry times (altitudes) for the same initial entry velocity. A similar trend in results was noted also for the gas composition of 99.5% N_2 + 0.5% CH_4 (ref. 17). For this composition, the radiative heating is negligible in comparison to the convective heating. One exception to this, however, is noted from the results presented in figure 11(b). The radiative heating rate for entry velocity of 13 km/sec is considerably higher than for other velocities. Thus, for the entry speed of 13 km/sec (and for entry times between 30 and 60 sec), it is possible to have physical conditions in the shock layer to produce a higher concentration of radiating species.

For the freestream atmospheric composition of 90% N_2 + 10% CH_4 , the results for stagnation-point convective and radiative heating are shown in figure 12 (and also in table 7) for Trajectories I and II. The results show that the extent of both convective and radiative heating is considerably higher for Trajectory I (a steeper entry angle trajectory) than for Trajectory II. This, however, would be expected because the rate of viscous dissipation will be higher for the steeper trajectory resulting in a relatively higher shock temperature.

For the atmospheric composition of 99.5% N_2 + 0.5% CH_4 , the variation of stagnation-point convective and radiative heating with body nose radius is given in figure 13 for Trajectory I and entry time 78 sec ($z = 50.9$ km). Although the extent of radiative heating is small, it is seen to increase with increasing nose radius. The convective rate, however, is seen to decrease with increasing nose radius. For a given set of entry conditions, the shock-standoff distance, in general, increases with increasing nose radius (ref. 9). This, in turn, results in different temperature, pressure, and species distribution in the shock layer. A combination of these changes influences the trend exhibited.

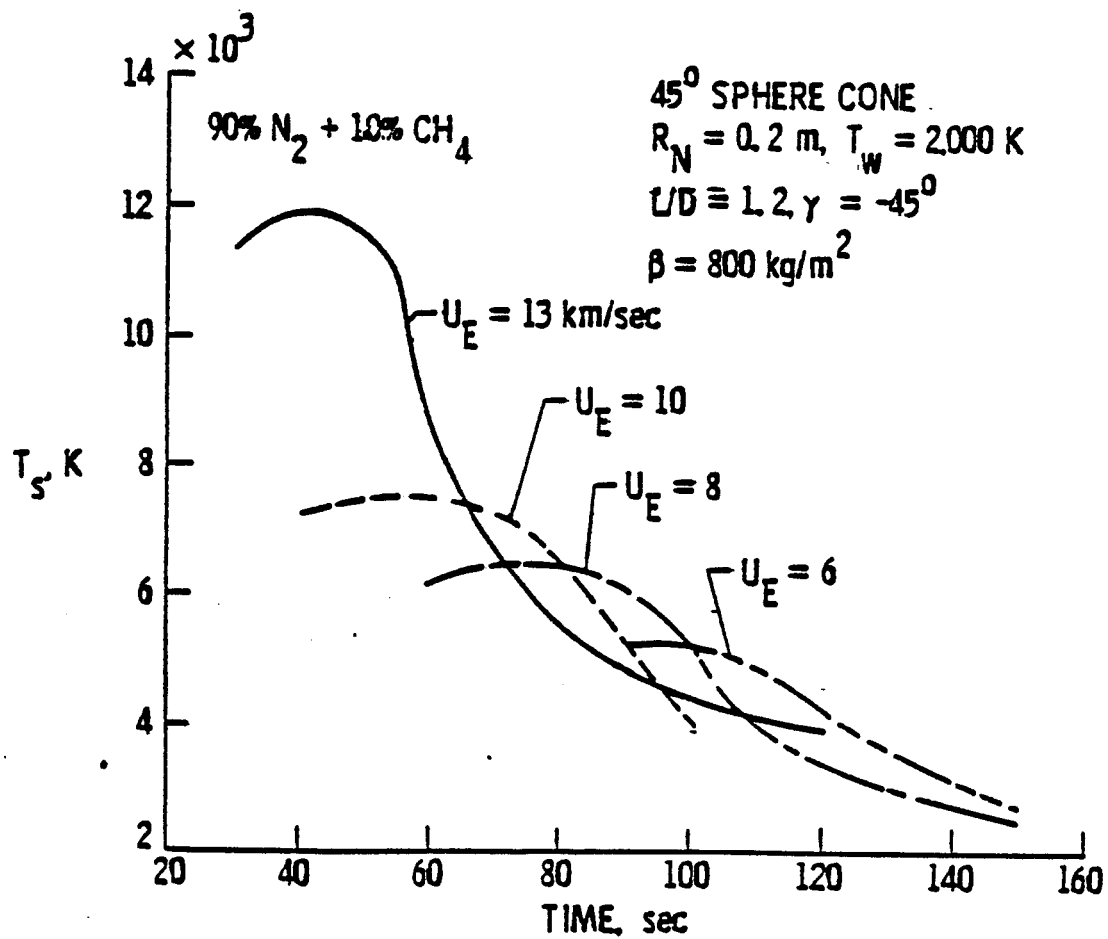


Figure 9. Effect of entry velocity on stagnation-point shock temperature, 90% N_2 + 10% CH_4 .

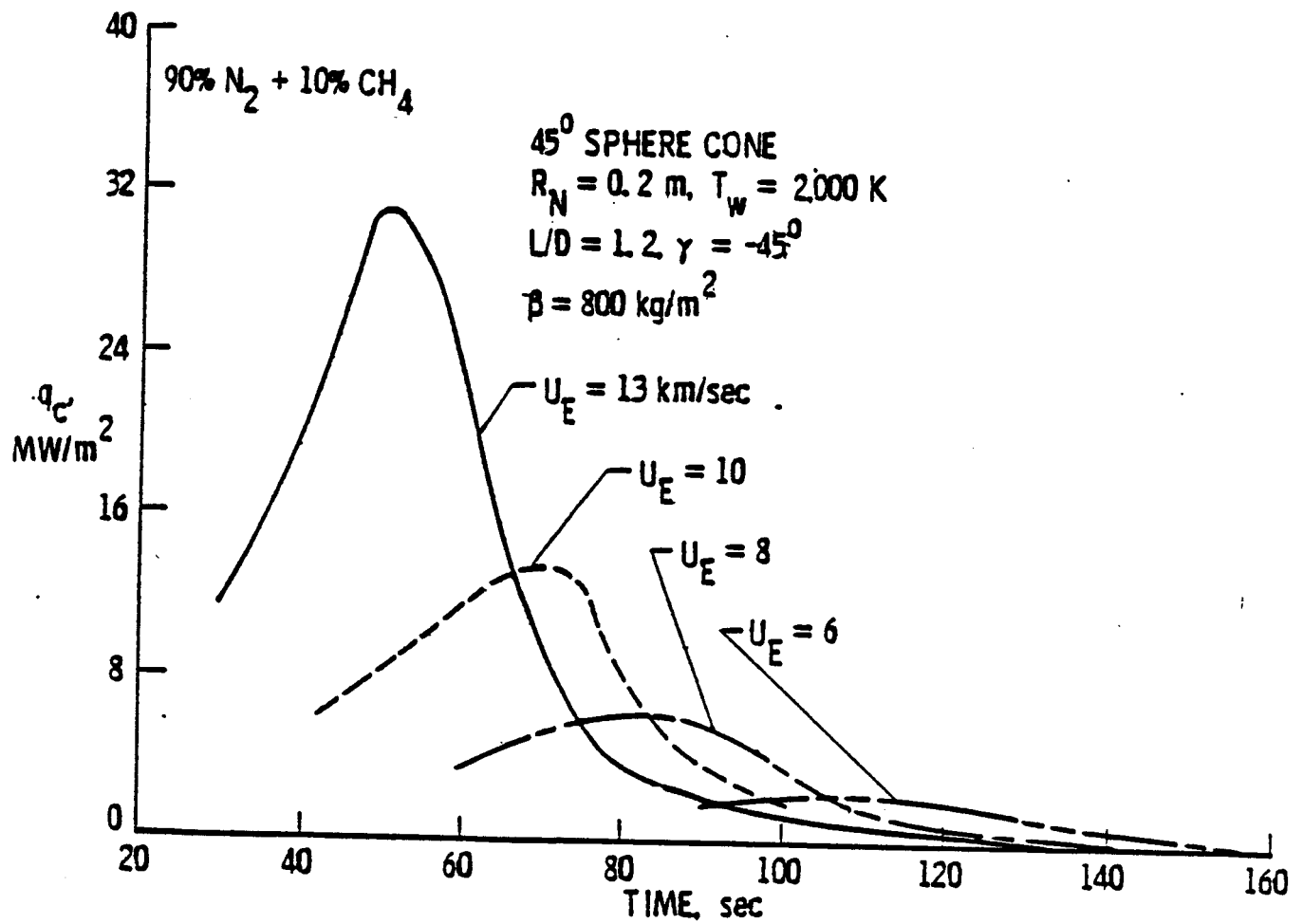


Figure 10. Effect of entry velocity on stagnation-point convective heating, 90% N₂ + 10% CH₄.

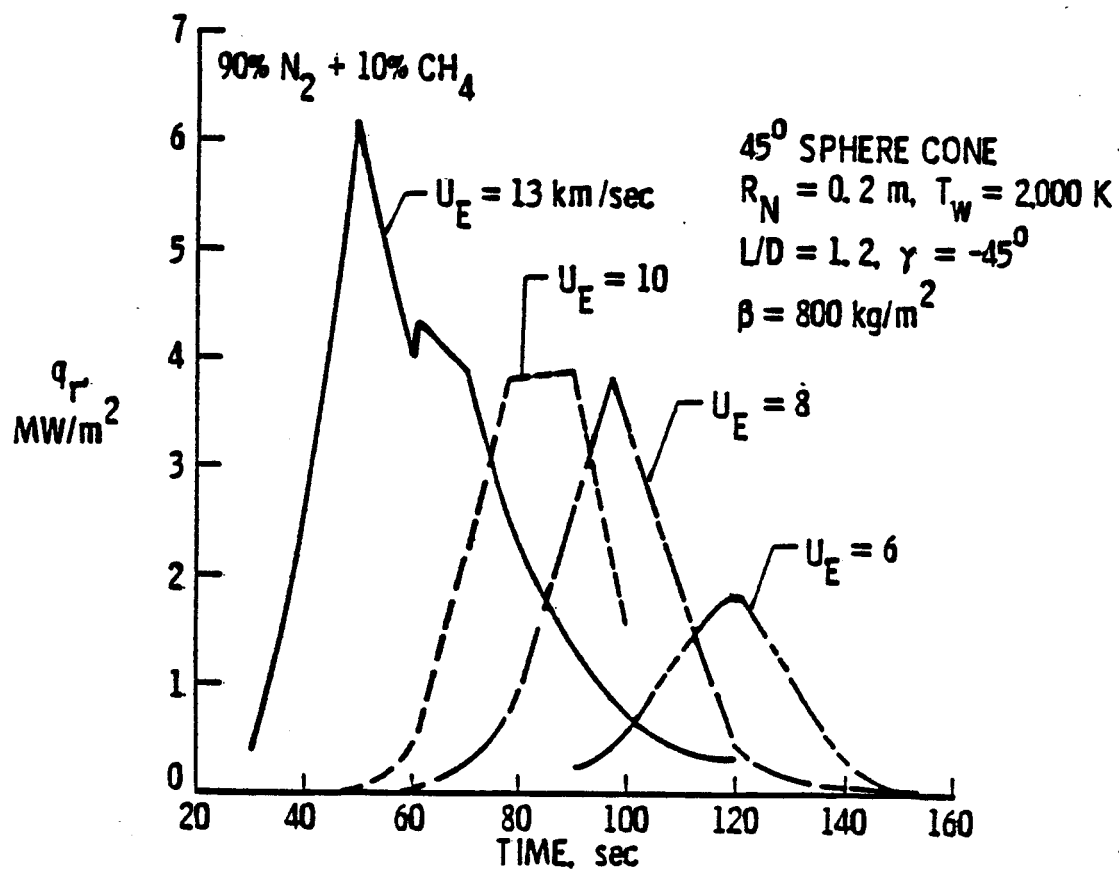


Figure 11(a). Effect of entry velocity on stagnation-point radiative heating, 90% N₂ + 10% CH₄.

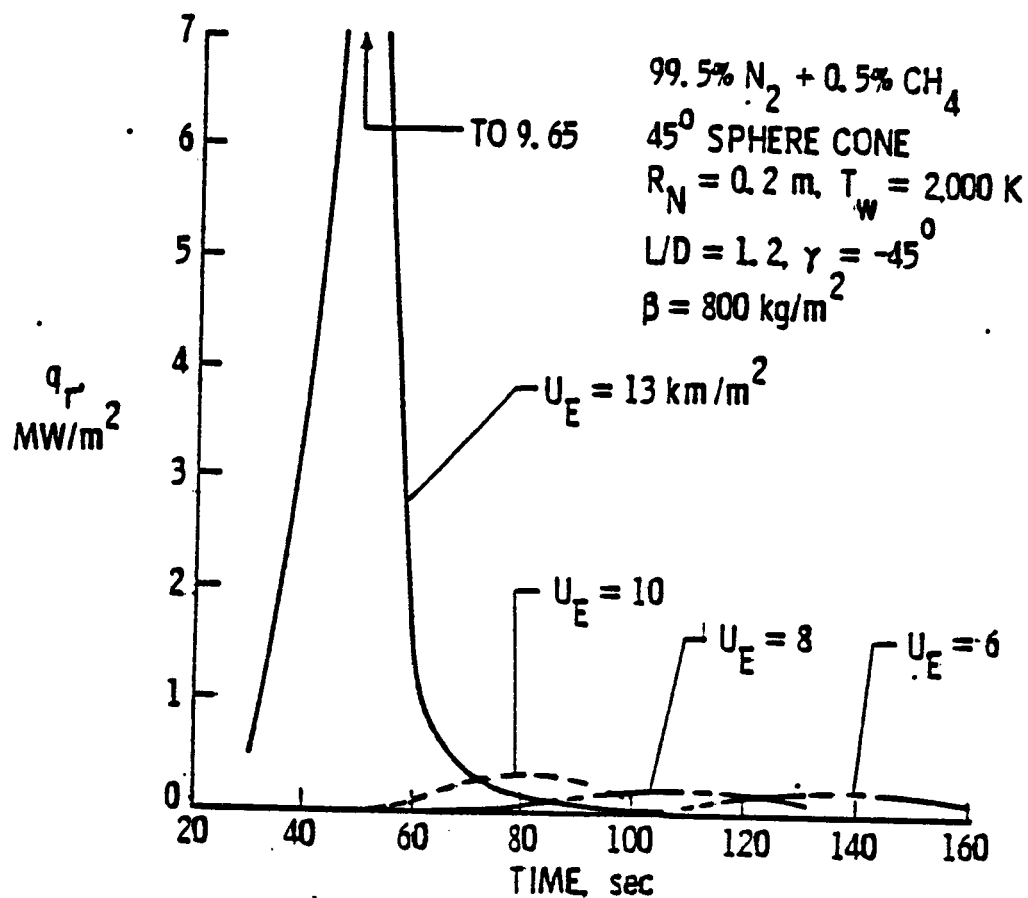


Figure 11(b). Effect of entry velocity on stagnation-point radiative heating, 99.5% N_2 + 0.5% CH_4 .

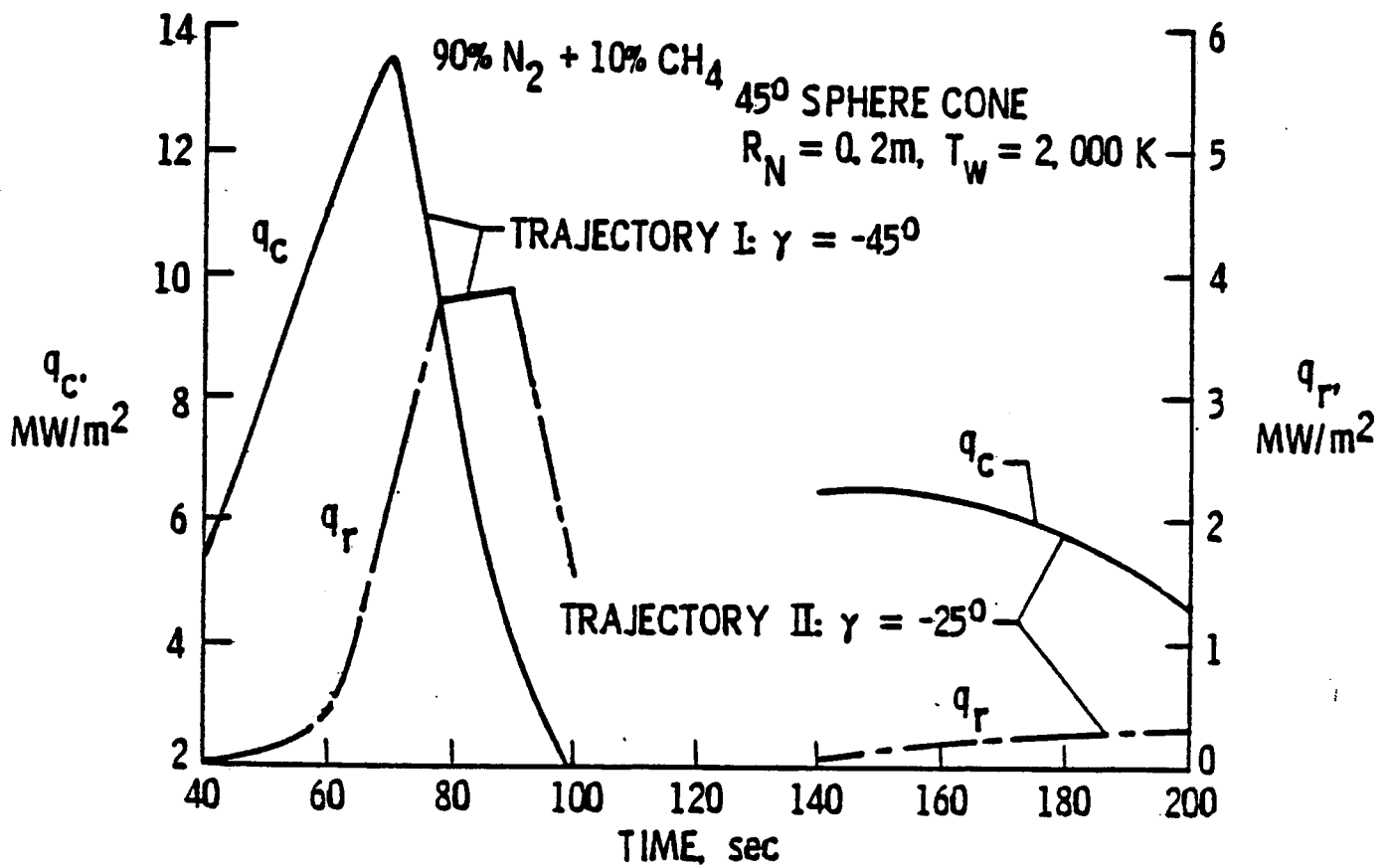


Figure 12. Variation of stagnation point convective and radiative heating for Trajectories I and II, 90% N₂ + 10% CH₄.

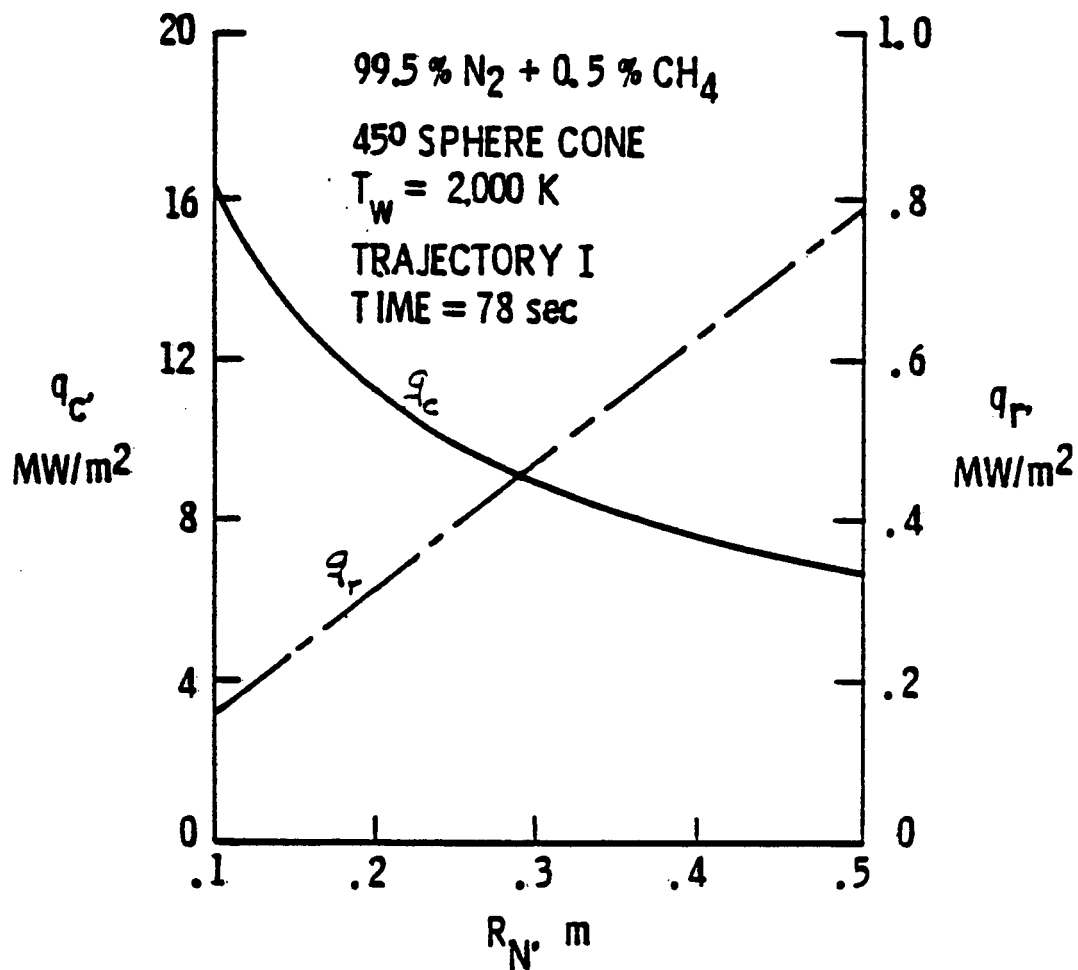


Figure 13. Effect of body nose radius on stagnation-point convective and radiative heating for 99.5% N₂ + 0.5% CH₄, t = 78 s.

The results of heating rate along the body are illustrated in figures 14 and 15 for Trajectory I and for the entry conditions at 78 sec. Variations in shock temperature and heating rates are shown in figure 14 for the atmospheric composition of 99.5% N_2 + 0.5% CH_4 . The results show that both convective and radiative heating essentially follow the trend of the shock temperature from the stagnation point to the tangency point (at about $s = 0.8$). Beyond this point, the convective heating continues the same trend but the radiative heating is seen to increase with the body location. This is because the pressure and temperature conditions near such locations are conducive for production of the radiating CN species over a larger portion of the shock-layer thickness (see fig. 3); and also because the optical thickness of the shock-layer gas is relatively higher in the downstream regions. The variation in heating rates along the body is illustrated in figure 15(a,b) for the cases with and without CN concentration in the shock-layer gas. The results show that while the presence of CN has little influence on the convective heating, the radiative heating is increased considerably by its presence. It is important to note that after the tangency point, the rate of radiative heating in the presence of CN is significantly higher than the convective heating for the freestream composition of 90% N_2 + 10% CH_4 , [fig. 15(a)]. The same trend is seen in figure 15(b) for the atmospheric composition of 99.5% N_2 + 0.5% CH_4 , but the extent of radiative heating is considerably small.

For the freestream atmospheric composition of 99.5% N_2 + 0.5% CH_4 , variations in important results with distance along the body surface are illustrated in figures 16-18 for Trajectory I and for critical entry times (altitudes). The results for shock density and shock-standoff distance presented in figure 16 show that, for a given entry altitude, the shock-standoff distance increases as density decreases. The shock-standoff distance is seen to decrease with increasing altitude; this is because higher freestream velocities are associated with higher altitudes (see table 1). The results for shock temperature and enthalpy presented in figure 17 show that both decrease along the body until the tangency point and they essentially remain constant beyond that point. Because of higher freestream velocities, the shock temperature and enthalpy are greater for higher altitudes. The variation in heating rates is shown in figure 18. As discussed

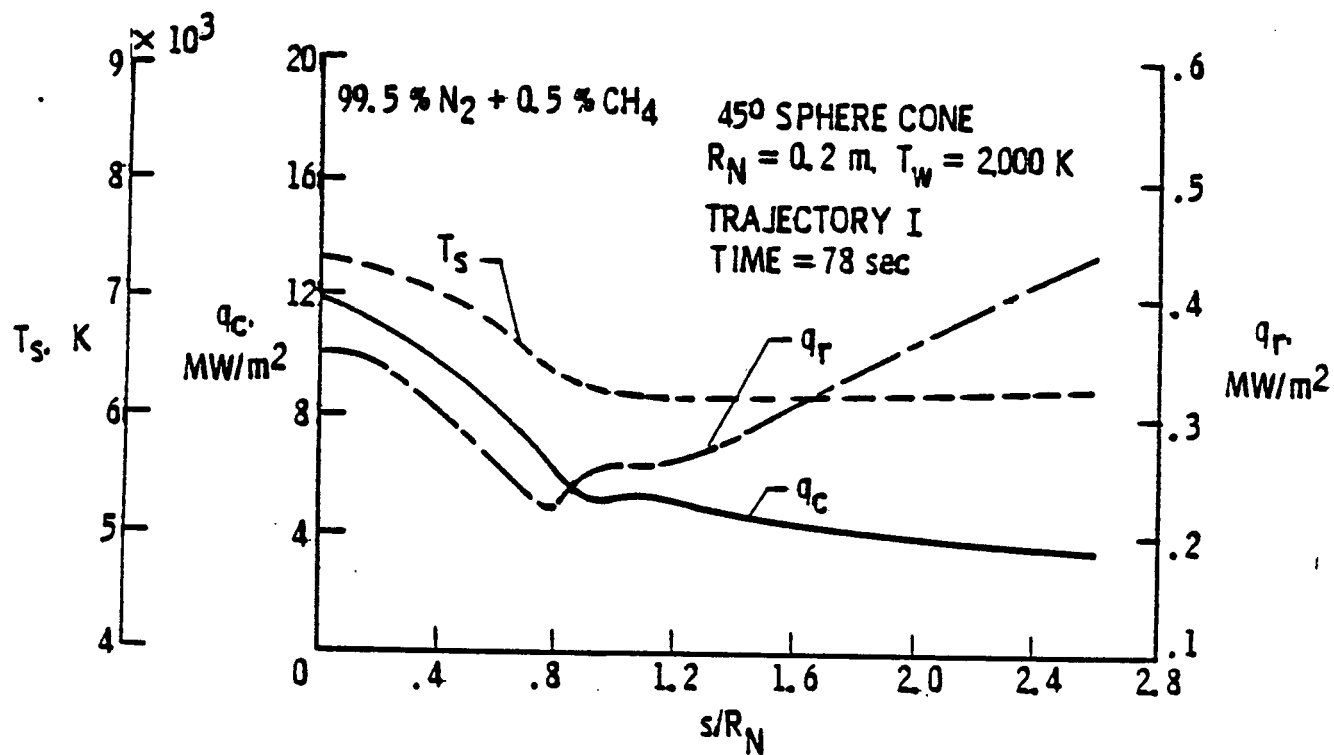


Figure 14. Variation of shock temperature, convective and radiative heating along the body for 99.5% N₂ + 0.5% CH₄.

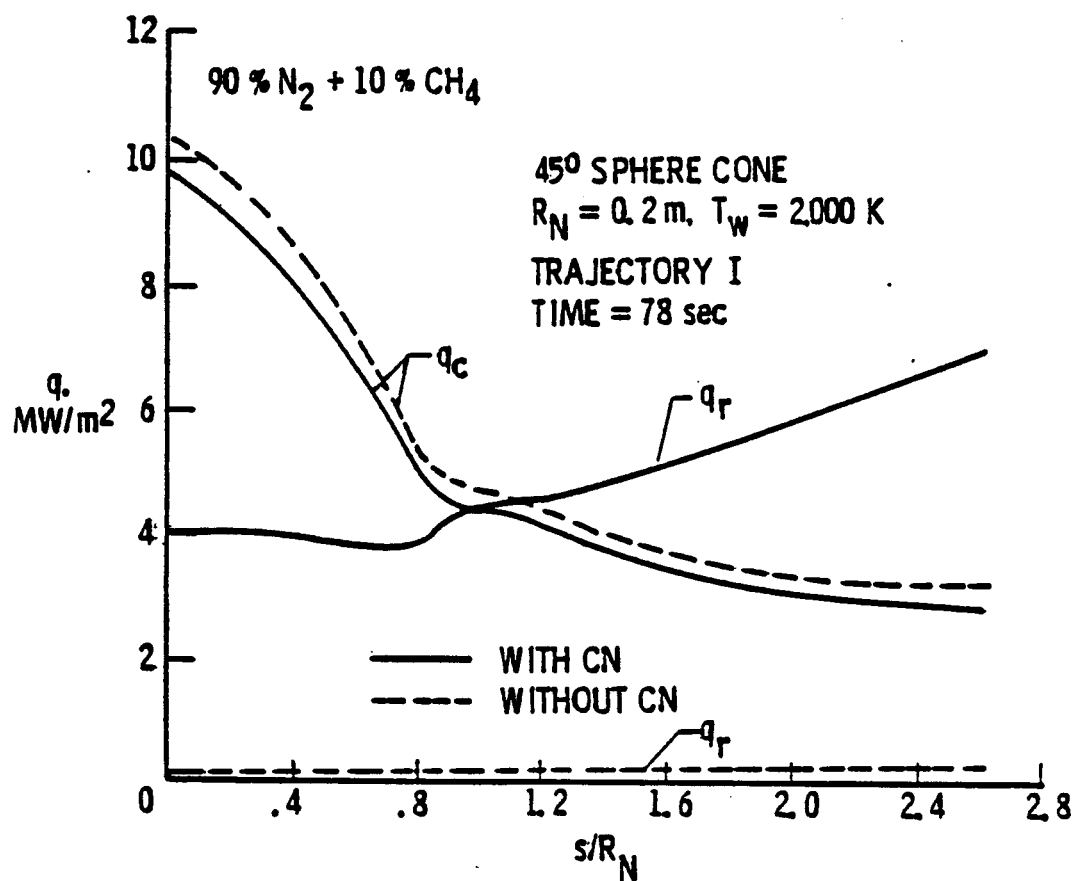


Figure 15(a). Influence of CN on convective and radiative heating along the body for $t = 78$ s and 90% N_2 + 10% CH_4 .

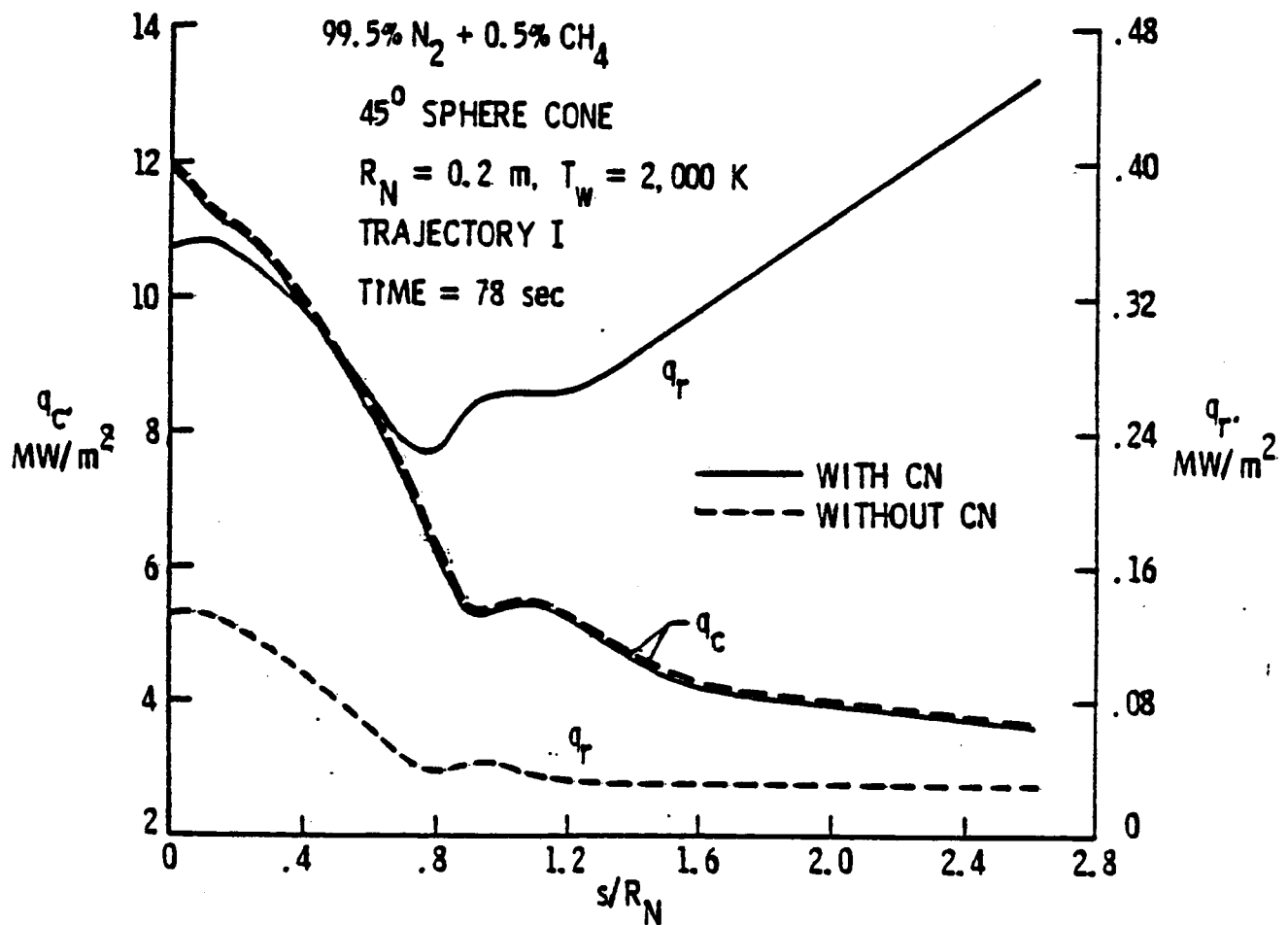


Figure 15(b). Influence of CN on convective and radiative heating along the body for $t = 78$ s and 99.5% N₂ + 0.5% CH₄.

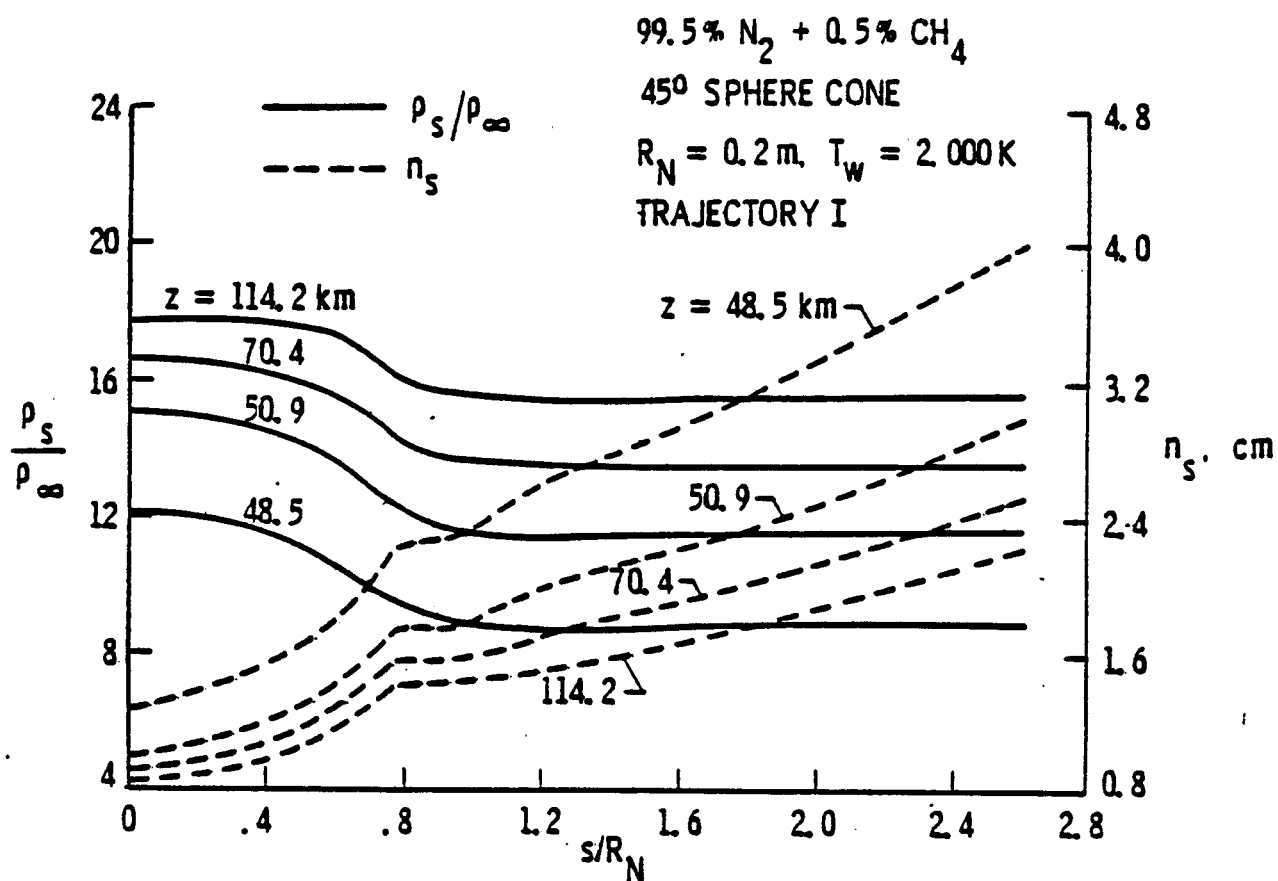


Figure 16. Variation of shock density and shock-standoff distance with body coordinate for 99.5% N₂ + 0.5% CH₄.

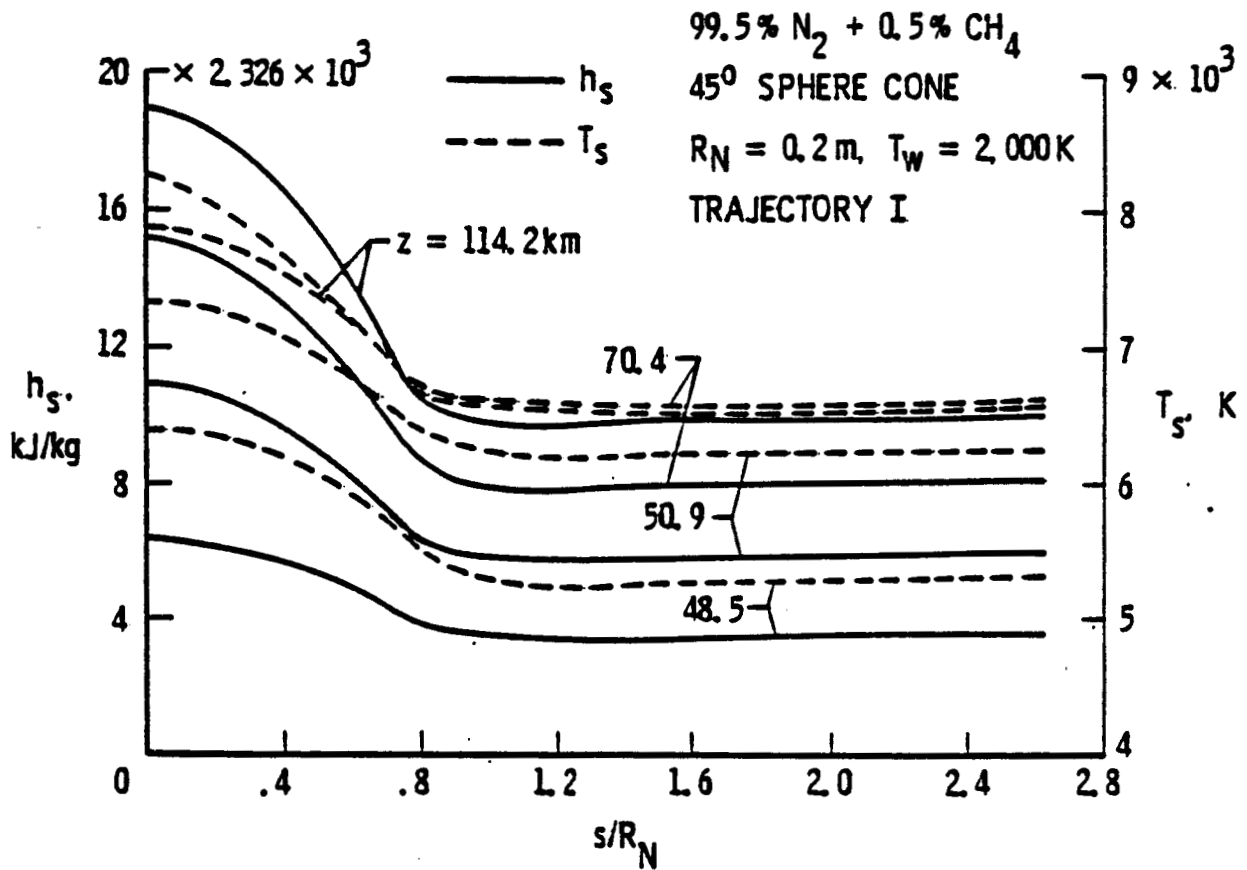


Figure 17. Variation of shock temperature and enthalpy with body coordinate for 99.5% N₂ + 0.5% CH₄.

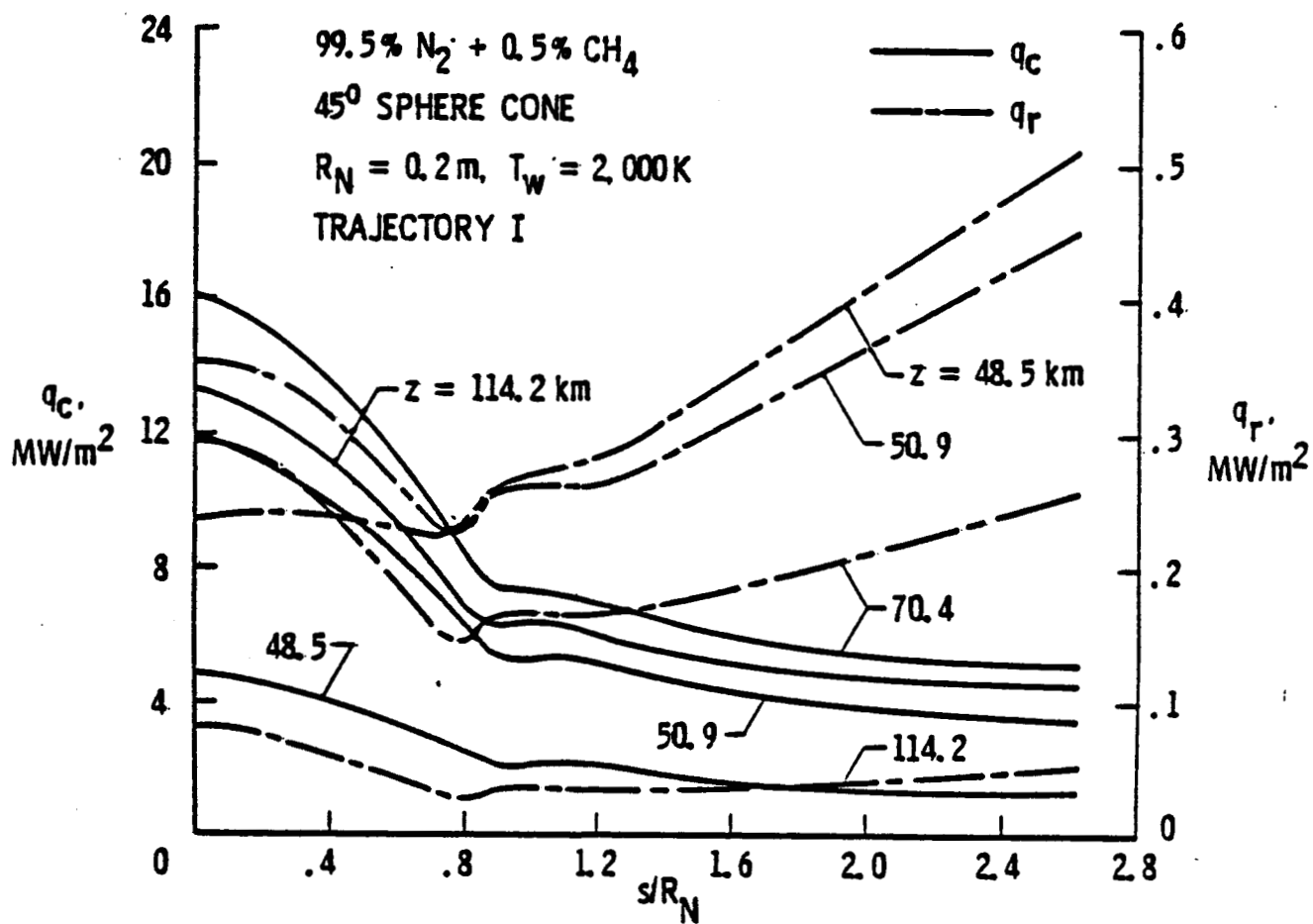


Figure 18. Variation of convective and radiative heating along the body for 99.5% N_2 + 0.5% CH_4 .

earlier, the peak convective heating occurs for entry conditions at $t = 78$ sec ($z = 70.4$ km) and peak radiative heating at $t = 78$ sec ($z = 50.9$ km). These results clearly show that in the stagnation region the radiative heating is not important if the Titan's atmospheric composition is considered to be 99.5% N_2 + 0.5 CH_4 .

The extent of convective and radiative heating over the entire length of the aerocapture vehicle is shown in figure 19 for the freestream-gas composition of 90% N_2 + 10% CH_4 . The results clearly show that while the convective heating rate continues to decrease in the downstream region, the radiative rate is considerably higher in this region. As discussed before, the reason for this trend is the combined influence of shock temperature, density and pressure variation in this region, and because of relatively higher optical thicknesses of the radiating shock layer. A similar trend in heating rates was noted also for the gas composition of 99.5% N_2 + 0.5% CH_4 (ref. 17), but the extent of radiative heating was found to be relatively lower.

CONCLUSIONS

Results were obtained to assess the extent of convective and radiative heating to an aerocapture vehicle for the Titan's aerocapture mission. Different compositions for the Titan's atmosphere were assumed and results were obtained for the entry trajectories specified by JPL. Specific results were obtained for the freestream atmospheric composition of 90% N_2 + 10% CH_4 and 99.5% N_2 + 0.5% CH_4 .

Results show that both the convective and radiative heating rates are quite sensitive to the gas composition used. The convective heating increases significantly as the N_2 concentration increases. However, this, in general, is not the case with regard to the radiative heating. The radiative heating is negligible for the shallow entry ($\gamma = -25^\circ$) condition regardless of the freestream gas composition. But, for the steepest entry angle ($\gamma = -45^\circ$), the radiative heating will be important only if the freestream gas is assumed to contain N_2 concentrations between 50% to 90%. For the gas composition of 90% N_2 , the radiative heating is important in the

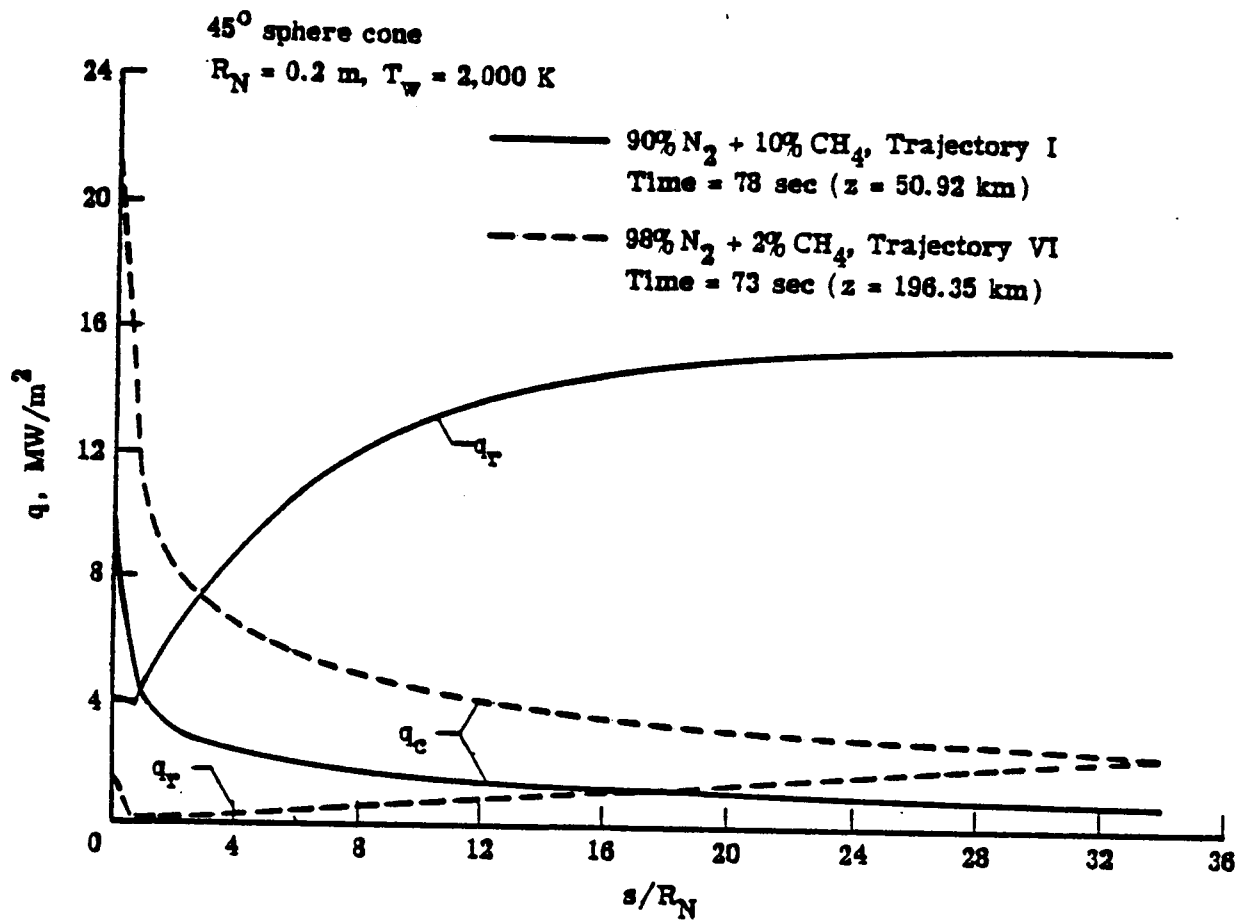


Figure 19. Variation of convective and radiative heating along the body for Trajectory I, 90% N_2 + 10% CH_4 ($t = 78 \text{ s}$), and Trajectory VI, 90% N_2 + 2% CH_4 ($t = 78 \text{ s}$).

stagnation region with the peak radiative rate being 30% of the corresponding convective heating rate (about 13 MW/m^2). For the freestream gas composition of 99.5% N_2 • 0.5% CH_4 , the radiative heating in the stagnation region was found to be negligible (less than 3%) in comparison to the convective heating for all cases considered. For this gas composition, the peak convective heating was found to be about 15 MW/m^2 . The amount of CN concentration in the shock-layer gas determines the extent of the radiative heating. For a given freestream gas composition, the radiative heating downstream of the stagnation region increases due to an increase in the CN concentration and the optical thickness of the shock layer.

Other results obtained in this study show that higher initial entry speeds produce higher shock temperatures which, in turn, result in higher heating rates. Results for the gas composition with 99.5% N_2 indicate that while the convective heating decreases, the radiative heating increases with increasing body nose radius.

Since the aerocapture vehicle is expected to traverse a part of its atmospheric flight in the transitional flow regime, it is suggested for further study to include both the shock and body slip conditions in the entire analysis. At this time, it might be advisable also to include the effects of nonequilibrium chemistry.

REFERENCES

1. Cruz, M.I.: Aerocapture Vehicle Mission Design Concept. AIAA Paper 79-0893, May 1979.
2. Cruz, M.I.: Aerocapture Vehicle Mission Design Concepts for the Inner and Outer Planets. AIAA Paper 79-115, June 1979.
3. Armento, R.F.: Mars Aerocapture Vehicle Definition Study Final Report. G.E. Document No. 79SDR2258, Sept. 1979.
4. French, J.R.; and Cruz, M.I.: Aerobraking and Aerocapture for Planetary Missions. Astronautics and Aeronautics, Feb. 1980, pp. 48-71.
5. Cruz, M.I.: Technology Requirements for a Generic Aerocapture System. AIAA Paper 80-1493, July 1980.
6. Florence, D.E.: Aerothermodynamic Design Feasibility of a Mars Aerocapture/Aeromaneuver Vehicle. AIAA Paper 81-0350, Jan. 1981.
7. Bird, R.B.; Stewart, W.E.; and Lightfoot, E.N.: Transport Phenomena. John Wiley & Sons, Inc., New York, 1960.
8. Moss, J.N.: Reacting Viscous-Shock-Layer Solutions with Multicomponent Diffusion and Mass Injection. NASA TR-411, June 1974.
9. Tiwari, S.N.; and Szema, K.Y.: Effects of Precursor Heating on Radiative and Chemically Reacting Viscous Flow Around a Jovian Entry Body. NASA CR-3186, Oct. 1979.
10. Moss, J.N.: Stagnation and Downstream Viscous-Shock-Layer Solution with Radiation and Coupled Ablation Injection. AIAA Paper 74-73, Jan. 1974; also AIAA Journal, Vol. 14, Sept. 1976, pp. 1311-1317.
11. Tiwari, S.N.; and Szema, K.Y.: Influence of Precursor Heating on Viscous Flow Around a Jovian Entry Body. Progress in Astronautics and Aeronautics: Outer Planet Entry Heating and Thermal Protection. Vol. 64, edited by R. Viskanta, AIAA, New York, 1979, pp. 80-107.
12. Davis, R.T.: Numerical Solution of the Hypersonic Viscous-Shock-Layer Equations. AIAA Journal, Vol. 8, May 1970, pp. 843-845.
13. Tiwari, S.N.; and Subramanian, S.V.: Influence of Nonequilibrium Radiation and Shape Change on Aerothermal Environment of a Jovian Entry Body, NASA CR-NSG 1500, Aug. 1980; also Ph.D. Dissertation by S.V. Subramanian, Old Dominion University, Norfolk, VA, March 1980.
14. Nicolet, W.E.: User's Manual for the Generalized Radiation Transfer Code (RAD/EQUIL). NASA CR-116353, Oct. 1969; also User's Manual for RAD/EQUIL/1973, A General Purpose Radiation Transport Program. NASA CR-132470, Nov. 1973.

15. Golden, F.: Visit to a Large Planet: A Thousand Rings Round Saturn, Icy Moons and Lakes of Liquid Nitrogen. Time Magazine, Vol. 116, No. 21, Nov. 24, 1980, pp. 32-41.
16. Stround, C.W.; and Brinkley, K.L.: Chemical Equilibrium of Ablation Materials Including Condensed Species. NASA TN D-5391, Aug. 1969.
17. Tiwari, S.N.; and Chow, H.: Aerothermodynamic Environment for a Titan Aerocapture Vehicle. NASA CR-NAG1-120, Jan. 1981.
18. Esch, D.D.; Siripong, A.; and Pike, R.W.: Thermodynamic Properties in Polynomial Form for Carbon, Hydrogen, Nitrogen, and Oxygen Systems From 300 to 15,000 K. NASA CR-111989, Nov. 1970.
19. McBride, B.J.; Heimerl, S.; Ehlers, J.G.; and Gordon, S.: Thermodynamic Properties to 6,000 K for 210 Substances Involving the First 18 Elements. NASA SP-3001, 1963.
20. Esch, D.D.; Pike, R.W.; Engel, C.K.; Farmer, R.C.; and Balhoff, J.F.: Stagnation Region Heating of a Phenolic-Nylon Ablator During Return from Planetary Missions. NASA CR-112026, Sept. 1971.
21. Grier, N.T.: Calculation of Transport Properties and Heat-Transfer Parameters of Dissociating Hydrogen. NASA TN D-1406, Oct. 1962.